University of Groningen

Characterization of the VeloPix Detector Gain Response to Fe-55 Irradiation

Masters's Thesis

To fulfill the requirements for the degree of
Master's in Physics
at University of Groningen under the supervision of
Dr. K.A.M. De Bruyn (Van Swinderen Institute, University of Groningen),
and
Prof. Dr. S. Hoekstra (Van Swinderen Institute, University of Groningen)

Alfonso Puicercus Gomez (s3938107)

July 24, 2024

Abstract

The LHCb experiment investigates the properties of subatomic particles, particularly focusing on heavy-flavour physics, thanks to the acceleration and collision of protons provided by the Large Hadron Collider (LHC). A new silicon pixel detector, known as the Vertex Locator (VELO), is currently being commissioned, with its calibration and optimisation being crucial for its correct operation at LHCb.

In pursuit of characterizing the Velopix, an Application-Specific Integrated Circuit (ASIC) which is a key component of the VELO's silicon pixel modules, controlled scenarios using exposure to a radiation source were used. A study on the energy deposition is presented, together with an exploration on the behaviour of the physical parameters of individual pixels is compared to that of the overall ASIC. This paper mainly investigates the conversion factor or gain K[e-/DAC], which is a relevant parameter for the operation of the detector. It provides a direct link between analog signal generated by electrons and the digital output, influencing the ability of the detector to convert the incoming particle signals into meaningful data when it is operational surrounding the collision point of the LHCb.

This thesis presents a detailed study on the calibration of the gain of the Velopix detector under irradiation from the quasi-monochromatic Fe55 source at two different operating temperatures. The gain was determined to be 14.33 $\pm$ 0.02 (stat) $\pm$ 0.16 (sys) [e-/DAC] at -20°C and 13.14 $\pm$ 0.01 (stat) $\pm$ 0.44 (sys) [e-/DAC] at 20°C, demonstrating a temperature dependence. The study also looked into the reliability of using the ASIC average flux as a predictor of the mean pixel gain, finding it to be a plausible method. Factors such as exposure time, positional bias of pixels and operating temperature are explored and identified as influential on the gain measurements. Furthermore, a comparison to the gain estimated on the Velopix ASIC paper [4] shows a compatibility within 2.07 σ of both results.

This research contributes valuable insights on the Velopix ASIC performance under varying conditions, offering the first measurements of gain from irradiation studies. These findings lay possible groundwork for future irradiation studies and further optimization of the detector.

Contents

1 Introduction

The Large Hadron Collider (LHC) is the largest particle accelerator in the world, built at the European Organisation for Nuclear Research (CERN). One of its various experiments, the LHC beauty (LHCb) experiment, was designed to study heavy-flavour physics, heavy ion collisions and perform high precision measurements of electroweak processes.

Various upgrades are planned to be performed on the detector throughout its lifetime. The LHC Run 1 (2010-2012) and Run 2 (2015-2018) were periods used for particle collisions and data collection. Some flavour physics observables are limited by data statistics, thus calling for larger datasets to further improve the already established measurements. This allows a higher level of precision and tests further the theoretical results derived from particle physics theories such as the Standard Model. To accomplish this, an increase in the number of collision events is desired and with it, an upgrade on various sub-detectors. This is referred to as the LHCb Upgrade I, see Ref. [1] for more information on the full upgrade.

The data taking process of the LHC starts with the acceleration of protons in two beams, each accelerating in opposite directions until the required energy is achieved. After the protons have been accelerated to relativistic speeds, they are collided (pp interactions). The exotic new particles and their decay products coming from the pp collision then travel through LHCb detector, consisting of various sub-detectors distributed along the z direction. The z axis is defined to be along the beam pipe, pointing towards the muon system. A schematic of the LHCb detector cross-section is shown in the figure below.

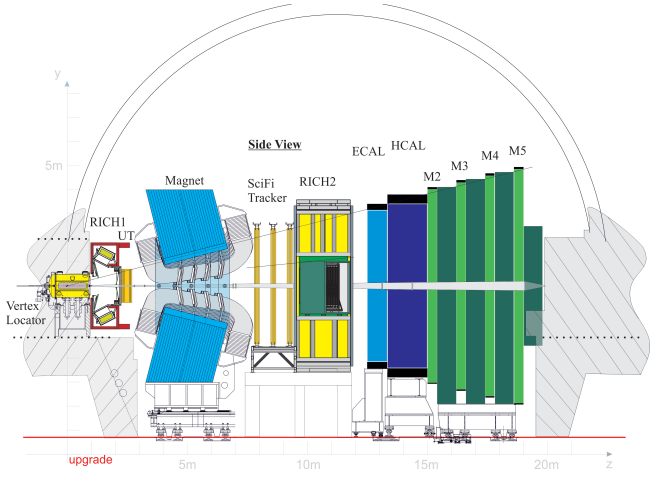

Figure 1: Layout of the upgraded LHCb detector [1].

The first sub-detector encountered by the daughter particles from the pp collision is the Vertex Locator (VELO), which is the silicon pixel detector that surrounds the interaction point. The LHCb Upgrade I implemented an upgraded version of the VELO, capable of withstanding the increase in luminosity expected to be delivered in LHCb Run 3-4. The calibration of a key component of the upgraded VELO will be the focus of this study.

1.1 Vertex Locator

The main purpose of the VELO detector is to measure the ionising particles' paths and, by reconstructing the tracks using algorithms, obtain information about the location of the primary and secondary vertices. These vertices correspond to the initial collision point of the protons and the decay points from unstable particles, respectively.

The VELO consists of 52 Modules distributed along the z axis, surrounding the interaction region as depicted in Fig. 2.

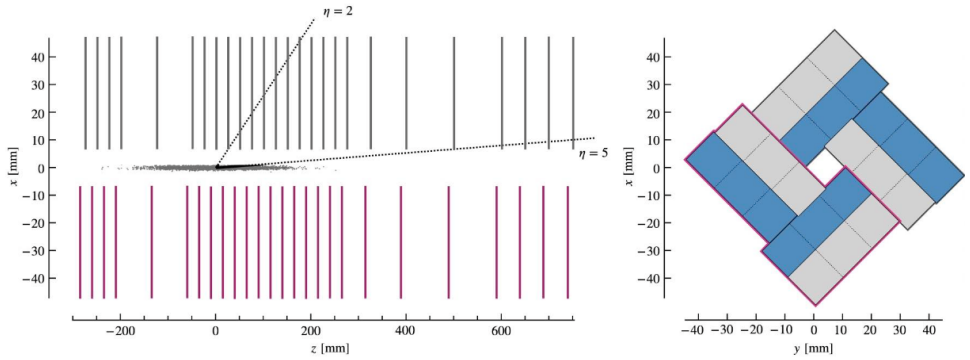

Figure 2: Left: Schematic top view of VELO showing the Module locations in the z–x plane. Right: Layout of the ASICs around the z axis in the closed configuration. The grey ASICs are placed on the upstream face, while the blue ASICs are those in the downstream face. Figure obtained from [1]

One Module contains 4 sensors, two per side. Each sensor contains 3 VeloPix, the name given to the Application-Specific Integrated Circuits (ASIC). A schematic of the detector and the ASICs layout is shown in Fig. 2 and Fig. 3 shows some key parts mentioned here. Each ASIC consists of a 256×256 grid of silicon pixels, with each pixel being 55×55 μm^2 in size and 200 μm thick. The Velopix also has a microchannel cooling system, which reduces the temperature of the ASICs when operational by using CO_2 at $-30°$ C. This operational temperature will also be referred to as Module temperature. The Velopix was developed based on the Timepix3 [2], thus sharing some of its characteristics. For further specific details on the characteristics of the Velopix refer to the LHCb Upgrade I publication [1].

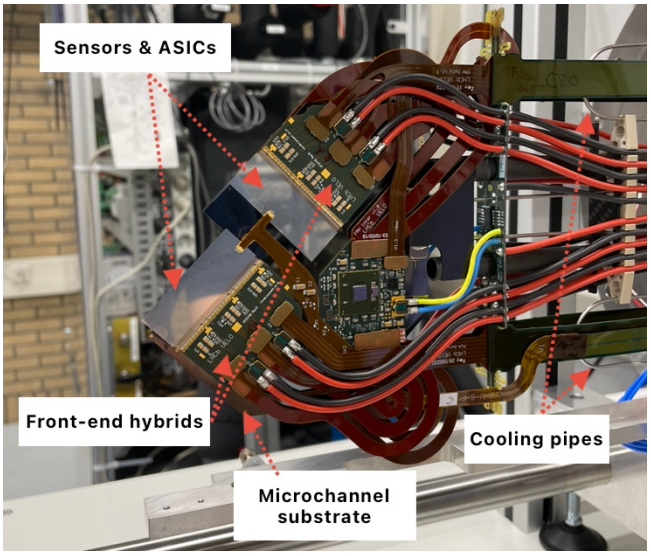

Figure 3: VELO Module used for data taking at Nikhef.

1.2 Characterization of the ASIC and objectives

The research project here presented aims to study the charge deposition in the detector, looking at the data from the standpoint of individual pixels and their average behaviour over the whole ASIC considered. This is achieved by using a controlled setup for the irradiation of the device.

From this, the mean pixel gain K[e-/DAC] is determined, crucial for a better understanding of the detector. It provides a relationship between the analog signal generated by incident particles, expressed in number of e^- collected, and the digital output from the ASIC, expressed in an arbitrary unit referred to as DAC. It is also useful to verify the uniformity of the individual pixels and balance noise rejection and detection efficiency.

Measurements on the Velopix have been performed by applying test pulses on one of the first Modules using the Speedy PIxel Detector Readout (SPIDR) developed at Nikhef [3]. This provided the characterization of some of the ASICs' attributes [4], presented in the table below. The given estimate from the test pulse study is K_{est} [mV/ke-] = 24.6. For a better comparison to the values found later on in this analysis, we convert this number to K_{est} [e-/DAC] = 15.45 ± 0.51, with the uncertainty inferred from the pixel to pixel gain variation shown in Table 1.2.

Pixel gain	24.6 mV / ke-
Pixel to pixel gain variation	3.3 %
Pixel ENC	62.9 e^-
Pixel to pixel threshold mismatch	410 e^-rms
Pixel to pixel threshold mismatch (calibrated, Threq)	40.3 e^-rms
Expected minimum threshold =6 $\sqrt{ENC^2 + \text{ Threq }^2}$	450 e^-

Table 1: Summary of the first measurements. Table obtained from [4]

Nevertheless, the test pulse study performed does not make use of measurements coming from direct energy deposition from irradiation, which makes the research here presented an important addition for the characterisation of the detector.

The analysis presented here exposed a VeloPix hybrid detector, consisting of sensor + readout ASIC, to a Fe55 source. The data was taken using the test setup designed for the quality assurance during the VELO module production, which partially took place at Nikhef in Amsterdam. The main objectives of the analysis are:

- Finding the gain K [e-/DAC] for the ASIC from the irradiation exposures to Fe55.
- Test whether one can say anything about the gain K of the individual pixels by considering only the overall flux on the ASIC.
- Explore possible effects and biases on the data in detail to provide insights on the characteristics and behaviour of the pixels and ASIC.
- Perform a comparison between the obtained mean gain and the estimate given by the first characterisation of the Velopix to determine the compatibility of the results.

2 Theory

2.1 Flux Models

2.1.1 Nominal Model

The flux received by an individual pixel of an ASIC exposed to a radiation source can be modelled using a Gaussian distribution with mean E_0 and width s,

$$f(E,s) \propto \frac{1}{s\sqrt{2\pi}} e^{-\frac{1}{2}\left(\frac{E-E0}{s}\right)^2} \tag{1}$$

A charged particle traversing the sensor deposits ionising radiation in a single pixel. Therefore, neighbouring pixels can receive a fraction f of the charge, this reflecting on the intensity equation above in the following way,

$$f(E,s,f) = (1-f)\cdot \frac{1}{s\sqrt{2\pi}} e^{-\frac{1}{2}\left(\frac{E-E0}{s}\right)^2} + f\cdot \frac{1}{2}\,\mathrm{erfc}\left(\frac{E-E0}{s}\right) \tag{2}$$

where f represents the charge sharing fraction and *erfc* is the complementary error function,

$$\mathrm{erfc}(x) = 1 - \frac{2}{\sqrt{\pi}}\int_0^x e^{-t^2} dt \tag{3}$$

often used to model asymmetrical broadening in the response function. The asymmetry arises from the measured decreasing energy spectrum, accounting for energy loss processes and other electronic effects [5].

The Velopix detects particle hits if the deposited charge is above a set threshold energy. Thus, to obtain the total flux received, one needs to integrate the differential flux $f(E,s,f)$ from said threshold to infinity.

$$F(E,s,f) = \int_E^\infty f(E',s,f)\; dE'$$

Since it is a quasi-monochromatic source of radiation used for this study, there is no need to integrate the intensity $f(E,s,f)$ over different wavelengths or frequencies. The total particle flux is then,

$$F(E,s,f) = Af\cdot\frac{1}{2}\left(\frac{s}{\sqrt{\pi}}e^{-\left(\frac{E-E0}{s}\right)^2} + (E0-E)\cdot\mathrm{erfc}\left(\frac{E-E0}{s}\right)\right) + A(1-f)\cdot\frac{1}{s\sqrt{8\pi}}\cdot\mathrm{erfc}\left(\frac{E-E0}{s\sqrt{2}}\right), \tag{4}$$

where A is the normalization factor to compensate for other effects not present in the model or setup specifics that were not accounted for during data taking.

The flux model here presented does not have a formal theoretical derivation, and it is empirically derived to approximate the shape observed in the data. The model contains information on the mean position E_0, but does not provide information on the energy deposition explicitly. To obtain the energy deposited it is necessary to delve deeper into the concept of thresholds, noise and the inner workings of the detector, explained in Sec. 2.2

2.1.2 Other Flux Models

Variations from the nominal flux model are considered to explore a possible better fit to the data. In this subsection, various flux equations will be explored. The original function is shown below for reference but introduced in 4. Note that a subscript has been added to the $F(E)$.

$$F_{1,0}(E) = Af\cdot\frac{1}{2}\left(\frac{s}{\sqrt{\pi}}e^{-\left(\frac{E-E0}{s}\right)^2} + (E0-E)\cdot\mathrm{erfc}\left(\frac{E-E0}{s}\right)\right) + A(1-f)\cdot\frac{1}{s\sqrt{8\pi}}\cdot\mathrm{erfc}\left(\frac{E-E0}{s\sqrt{2}}\right) \tag{5}$$

where the 1 denotes this is the nominal flux model together with the use of one s parameter, and ,0 points out the inclusion of the first Gaussian term or 0th term in the equation, which remains very small for further calculations in this analysis. However, it was still included and will be used to study some effects observed in

the data analysis.

$$F_1(E) = Af \cdot \frac{1}{2}(E0 - E) \cdot \text{erfc}\left(\frac{E - E0}{s}\right) + A(1-f) \cdot \frac{1}{s\sqrt{8\pi}} \cdot \text{erfc}\left(\frac{E - E0}{s\sqrt{2}}\right) \tag{6}$$

From a mathematical point of view, it could be advantageous to decouple the normalisation of the two terms. Therefore, two new scaling factors A^* and B^* are introduced into a new flux model, substituting the A and f variables,

$$A^* = \frac{1}{2}fA, \quad B^* = \frac{1}{2}(1-f)A \tag{7}$$

The flux equations below are the same as $F_{1,0}$ in Eq. 4, but using A^* and B^* as introduced above. The $F_{AB,0}$ notation uses AB, as the code name given to this flux equation and to its results.

$$F_{AB,0}(E) = A^* \cdot \left(\frac{s}{\sqrt{\pi}} e^{-\left(\frac{E-E0}{s}\right)^2} + (E0 - E) \cdot \text{erfc}\left(\frac{E - E0}{s}\right)\right) + B^* \cdot \frac{1}{s\sqrt{2\pi}} \cdot \text{erfc}\left(\frac{E - E0}{s\sqrt{2}}\right) \tag{8}$$

$$F_{AB}(E) = A^* \cdot (E0 - E)\,\text{erfc}\left(\frac{E - E0}{s}\right) + B^* \cdot \frac{1}{s\sqrt{2\pi}} \cdot \text{erfc}\left(\frac{E - E0}{s\sqrt{2}}\right) \tag{9}$$

It is important to reassert that in this new flux equations, the terms become more independent than those considered in F_1. Comparing the results coming from these two flux equations $F_{AB,0}$ and F_AB to that of the original equation, Eq. 4, will provide insights on the effect of these new scaling parameters in the fitting and categorisation of pixels.

Another possible scenario which can be considered is that the third term in the equation takes a different parameter s than that of the other first two terms, thus the flux equation would have the following form after implementing s_1 and s_2:

$$F_{2s,0}(E) = Af \cdot \frac{1}{2}\left(\frac{s_1}{\sqrt{\pi}} e^{-\left(\frac{E-E0}{s_1}\right)^2} + (E0 - E) \cdot \text{erfc}\left(\frac{E - E0}{s_1}\right)\right) + A(1-f) \cdot \frac{1}{s_2\sqrt{8\pi}} \cdot \text{erfc}\left(\frac{E - E0}{s_2\sqrt{2}}\right) \tag{10}$$

Two extra flux equations related to $F_{2s,0}$ are also considered, this being F_{2s}, which as the subscript indicates does not include term0, and an additional flux equation with double s parameters, this time denoted as $F_{2s,AB}$, making use of the scaling factors A^* and B^* recently introduced.

$$F_{2s}(E) = \frac{1}{2}fA \cdot (E0 - E)\,\text{erfc}\left(\frac{E - E0}{s_1}\right) + \frac{1}{2}(1-f)A \cdot \frac{1}{s_2\sqrt{2\pi}} \cdot \text{erfc}\left(\frac{E - E0}{s_2\sqrt{2}}\right) \tag{11}$$

$$F_{2s,AB}(E) = A^* \cdot (E0 - E) \cdot \text{erfc}\left(\frac{E - E0}{s_1}\right) + B^* \cdot \frac{1}{s_2\sqrt{2\pi}} \cdot \text{erfc}\left(\frac{E - E0}{s_2\sqrt{2}}\right) \tag{12}$$

An additional flux equation that implements two scaling factors A and B as well as an f and two s parameters to the nominal model is shown below:

$$F_{2s,AB,f}(E) = \frac{1}{2}fA \cdot (E0 - E) \cdot \text{erfc}\left(\frac{E - E0}{s_1}\right) + \frac{1}{2}(1-f)B \cdot \frac{1}{s_2\sqrt{2\pi}} \cdot \text{erfc}\left(\frac{E - E0}{s_2\sqrt{2}}\right) \tag{13}$$

2.2 Noise, thresholds and the equalisation process

Even when the ASICs are not exposed to radiation, there is a small current being measured, which corresponds to the electronic noise due to fluctuations within the pixels and the electronics involved. A schematic of said noise can be found below.

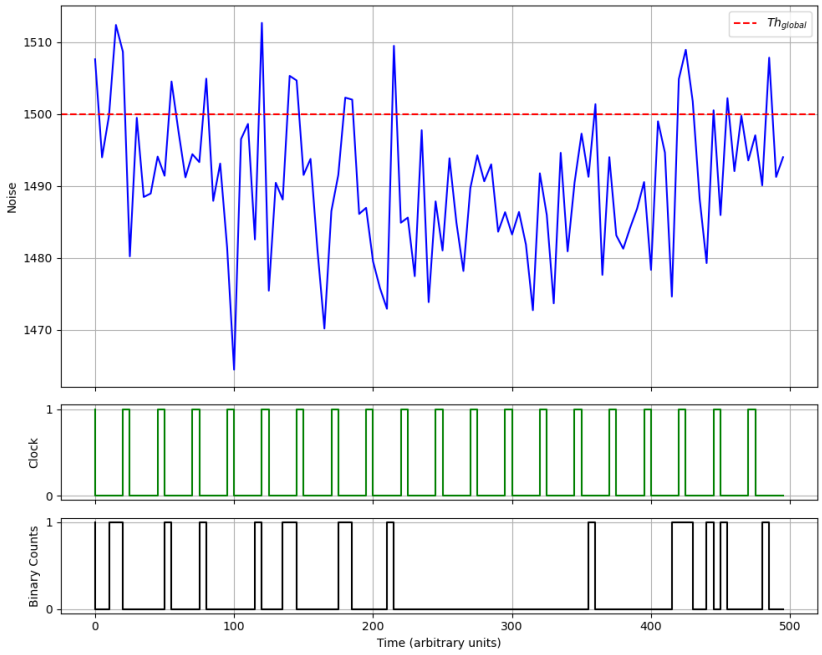

Figure 4: Noise schematic of ASIC showing clock ticks every 25 ns and the binary readout based on Th_{global} comparison.

This would be an example of the noise from a pixel. The first subplot, labelled as Noise, shows on the y-axis a schematic of the current that emanates from the noise of a pixel. The noise baseline E_b is the non-zero DAC (Digital-to-Analog Converter) value or threshold at which the pixels record maximal noise, mainly coming from fluctuations within them. The DAC values are the internal measurement units used by the Velopix detector for thresholds and measuring signal levels.

The global threshold Th_{global} is represented as a horizontal red line at a certain DAC value. This threshold is necessary for the pixel to decide what is recorded as a particle hit or not. This can be seen from the binary readout in Fig. 4 corresponding to the peaks of the current which lie above this set DAC. The transition from the analog to digital signal can be understood better with the following schematic.

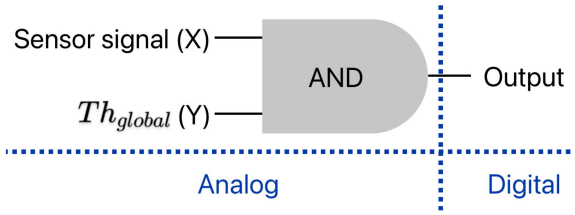

Figure 5: Schematic of signal comparison within a Velopix pixel. Signal_{input} refers to the signal from the pixel. Portrays the conversion from analog to digital signal.

If the ionisation from the passing particle is shared among pixels, the charge collected per pixel is lower. Thus, a global threshold that is too high would imply ignoring peaks in the current which are due to actual hits. Setting Th_{global} too low would imply picking up too much noise. Thus, it is key to find a proper value for this parameter.

The Velopix only has one global threshold Th_{global} by design. Nevertheless, although there is a careful examination in the manufacturing of the ASICs, individual pixels tend to have a small shift in the position of their noise. Some potential causes for the noise position variation from pixel to pixel might be small differences in size and imperfections, material impurities, thermal fluctuations, their position with respect to other electronics, etc.

The pixels within the ASICs only have one free configuration setting in order for their noise baseline position to be set around the same value. This setting is called *Trim*, which can take 16 different values labelled from 0 to F. These values can be understood better as a current offset added to the input signal from the pixel. If this signal including the Trim offset is greater than the global threshold Th_{global}, a hit is recorded, as shown in Fig. 5.

The equalisation process is the procedure by which it is possible to set the noise baseline position of the pixels to be around the same DAC value. This is to ensure that the pixels have almost the same response when the detector is operational. The equalisation process is not the scope of this study, but the concepts and results obtained from it are relevant, since they are involved in the analysis performed. The equalisation process returns three main results:

1. Trim setting matrix

2. Global Threshold for the ASIC

3. Masked Pixel matrix

To mask pixels that have anomalous behaviour or are not working, the masked pixel matrix is used in this analysis.

A better understanding of the concept of thresholds can be obtained from the graphs below. Figure 6 represents a Velopix ASIC exposed to the Fe55 source. The recorded hits per second are shown as a function of Th_{global}. A high peak in flux is observed at around 1400 DAC which corresponds to the noise baseline position E_b, set approximately between 1375 and 1425 DAC, around the threshold range at which pixels maximally record hits coming from the noise fluctuations.

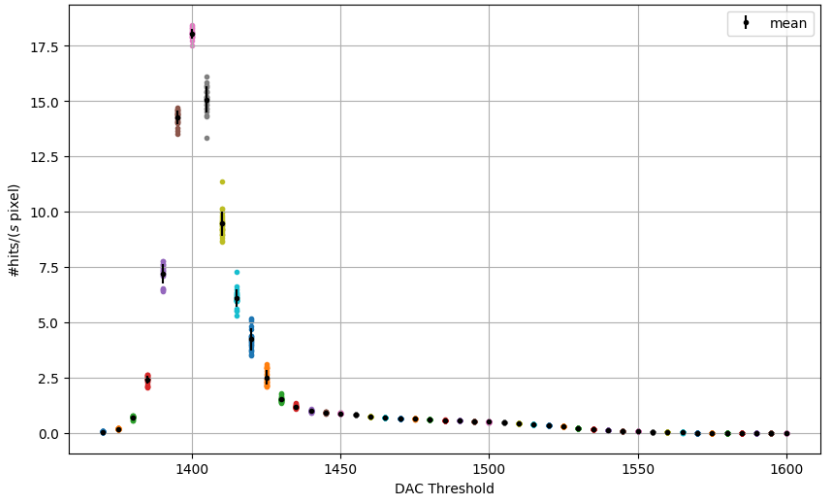

Figure 6: Flux vs threshold scan for a Velopix ASIC exposed to a source.

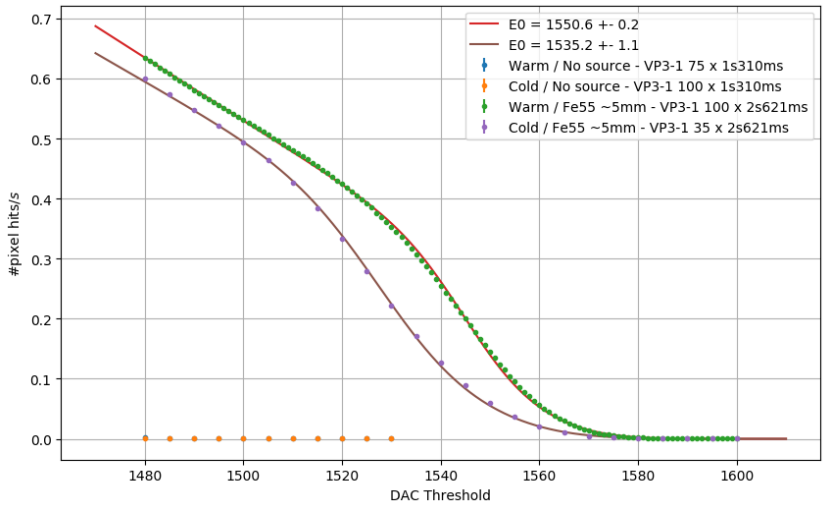

Figure 7: Flux vs threshold plot with and without source. Threshold axis rescaled to show the range where drop in flux occurs due to the radiation source.

There is a slight drop in flux in the higher DAC range, which occurs due to the particles coming from the radiation source used, but it is barely noticeable unless the graph is rescaled to that of Fig. 7. It is located in between 1500-1550 DAC, and it corresponds to the threshold E_0, previously introduced within the flux model in Eq. 4. As it can be seen from the figure, the data which does not have a source, presents 0 flux and thus the data points directly lie on the x-axis, whereas the datasets with a source have a non-zero flux, as expected.

So far, two *special* thresholds have been introduced in this section, these being E_b and Th_{global}. Moreover, by using the E_0 introduced in the flux model in Eq. 4, the energy deposition on the pixel from the ionising particle can be obtained. The energy deposition in DAC units will be referred to as *target*, $E_t = E_0 - E_b$ found with difference of E_0 and the noise baseline E_b. This can be done since the noise baseline position E_b represents 0 energy deposited in the sensor, while the E_0 is determined from a fit to the flux over threshold DAC distribution.

2.3 Source

The source of radiation used is Fe55, which decays with a half-life of 2.74 years with 100% probability to Mn55 by electron capture (EC). The emissions expected are listed in the table below.

#	E [keV]	I(abs) [%]	Line
1	$0.556 - 0.764$	0.66 *10*	L
2	5.888	8.45 *16*	$K - L_2$
3	5.899	16.6 *3*	$K - L_3$
4	$6.489 - 6.535$	3.40 *7*	$K - MN$
5	$6.489 - 6.535$	3.40 *7*	$K - M_{2,3,4}$

Figure 8: Details on X-ray decay modes from Fe55. Obtained from [6].

The most relevant X-ray emission is the Mn Kα X-ray at around 5.9 keV (combining this way the K-L2 and K-L3 lines shown in the table). There is also a weaker Mn Kβ X-ray, not expected to be measured. Other decay modes include the emission of gamma radiation and Auger electrons. These electrons have an energy of a few keV and are expected to be absorbed within the enclosure of the source. Thus, the Velopix ASIC will be irradiated with the quasi-monochromatic source Fe55, predominantly by $E_\gamma = 5.9$ keV X-rays.

2.4 Detection Process

The emitted X-ray undergoes the photoelectric effect, therefore transferring its total energy to the atom, which then emits a shell electron. It is the dominant photon interaction process at energies in the lower keV range, typically above 1 keV [7]. For this process to occur, the incident particle has to lose some of its energy to excite an electron, which corresponds to the band gap energy $E_{bandgap}$. Thus, the energy of this photoelectron will be slightly less than the energy of the incident particle, calculated by,

$$E = E_\gamma - E_{bandgap}$$

Since the band gap energy for the silicon detector in use is $E_{bandgap} = 1.12$ eV, this being substantially smaller than E_γ, it was not included in the calculations and $E \approx E_\gamma$. Therefore, from this process, the X-ray photon has converted all its energy to a photoelectron. This photoelectron, being a charged particle travelling through the detector, can now create electron-hole pairs (ehp) which then become a measurable current.

When an energetic charged particle goes through a pixel, it creates the so-called electron-hole pairs (ehp), as it can be seen from the schematic cross-section of a Velopix pixel below:

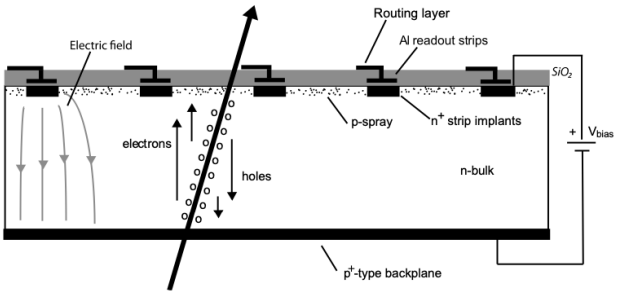

Figure 9: Cross-section of a VELO silicon pixel of type n-on-n. The pn-junction is formed at the interface of the backplane and the bulk. [8]

An electric field is applied between the backplane and the implants shown in Fig. 9, such that if an ionising particle travels through the bulk, electrons will drift towards the implant side, inducing a signal on the strips provided that they did not recombine during the process.

The average energy to produce an ehp by a charged particle, E_{ehp}, is dependent on the intrinsic properties of the medium and its temperature. Only an average can be specified due to random phonons being produced which take away part of the energy. One can find that for a detector made of Si, at room temperature $E_{ehp} = 3.69 \pm 0.11$ eV/ehp [9]. This parameter has been observed to increase, but at significantly lower temperatures [10]. Since the detector operated at -20°C during data taking, the value used throughout this study is $E_{ehp} = 3.69 \pm 0.11$ eV/ehp.

Taking the energy from the irradiated particle $E_\gamma = 5.9$ keV, and dividing by $E_{ehp} = 3.69$ eV should lead to the average number of ehp created in the pixel, assuming that the photoelectron is fully stopped in the pixel thickness:

$$n_{ehp} = \frac{E_\gamma}{E_{ehp}} = \frac{5900 \text{ eV}}{3.69 \text{ eV/ehp}} = 1598.92 \text{ ehp} \tag{14}$$

This means that every incident X-ray from our Fe55 radiation source will create an average of 1598.92 electrons. These electrons will then drift towards the read-out and induce an electric signal measured by the ASIC. We should expect every pixel to release the same amount of electrons per hit, however pixel-to-pixel variations due to impurities in the silicon or fluctuations within the pixel might slightly change this value.

2.5 Gain K[e-/DAC]

Both the number of electrons released within the pixel and the measured target E_t in DAC units by the detector should be related to the energy deposition on the pixel. Thus, we can divide the number of electrons $n_{e-} = n_{ehp}$, by the target so that the gain or conversion factor between e- and DAC units can be found:

$$K\left[\frac{e^-}{DAC}\right] = \frac{n_{e^-}}{E_t} = \frac{E_\gamma}{E_{ehp}}\frac{1}{(E_0 - E_b)} \tag{15}$$

From the above relationship, it can be concluded that as E_0 increases, so does E_t and thus, the value of K decreases. We will come back to this specific relation between E_0 and K later in the analysis.

The conversion factor here derived can be used to have a better understanding of the detector. It provides a direct equivalence between a number of electrons [e-] and a digital value in [DAC], associating the analog signal amplitude that would be produced by the released electrons within the depletion zone and the digital value which will be assigned by the electronics.

The objective of this study is to characterize the gain $K[e - /DAC]$ of the Velopix pixels and study their behaviour to irradiation. On the Velopix ASIC design paper [4], the estimation from test pulses found a gain of K_{est} [e-/DAC] $= 15.45 \pm 0.51$, with the analysis here shown aimed to compare this value with results obtained from measurements on energy deposition.

3 Data and other specifics

3.1 Datasets and data acquisition

Two datasets were used for this analysis, these differing on exposure time to the source and the operating temperature of the ASICs. The datasets used here are exposures of the ASIC labelled "VP3-1" to a quasi-monochromatic Fe55 radiation source with an operational temperature of $-20°C$ and another one at room temperature, labelled *cold* and *warm* respectively. The Module is cooled down throughout the data taking process to prevent it from overheating while operating, thus, labels aforementioned refer to the temperature acquired by the Module, not the actual usage of the cooling system since this is always active.

The datasets here presented make use of the MiniDAQ2, which is a data acquisition system designed for testing and debugging the LHCb detector components and electronics. Also, the "Module production" equalisation is utilized, developed and used during module construction and qualification prior to the installation of the detector. Since the module construction finished, the equalisation process has been studied in detail and its algorithm improved. However, it needs a newer version of the read-out firmware, which is not available on the MiniDAQ2 used here.

The table below compiles the relevant data acquisition information of the two datasets used for this analysis.

Set	Label	Module Temp.	ASIC	Shutter Time	nacq	Thr_{min}	Thr_{max}	Thr_{step}	Total time (h)
1	Cold	$-20°C$	VP3-1	2 s621 ms	50	1480	1600	1	4.36
2	Warm	$+20°C$	VP3-1	2 s621 ms	100	1480	1600	1	8.73

Table 2: Details concerning the two data sets.

The Shutter Time (ST) refers to the amount of time the ASIC is exposed per acquisition, *nacq* is the number of acquisitions per threshold considered, Thr_{min} and Thr_{max} are the extremes of the threshold scan range, together with Thr_{step} which defines the step size in DAC units taken in the scan. The Total time represents the exposure time of the dataset, and it is indicative of the quantity of data obtained. Note that not all thresholds and acquisitions are used, for reasons explained in Sec. 3.2. The total exposure time can be calculated using the following formula,

$$t = \frac{Thr_{max} - Thr_{min}}{Thr_{step}} \cdot \text{nacq} \cdot \text{ST} \tag{16}$$

The figures below represent the total flux over all thresholds measured by the VP3-1 ASIC to Fe55 irradiation for both the *cold* and *warm* dataset, respectively.

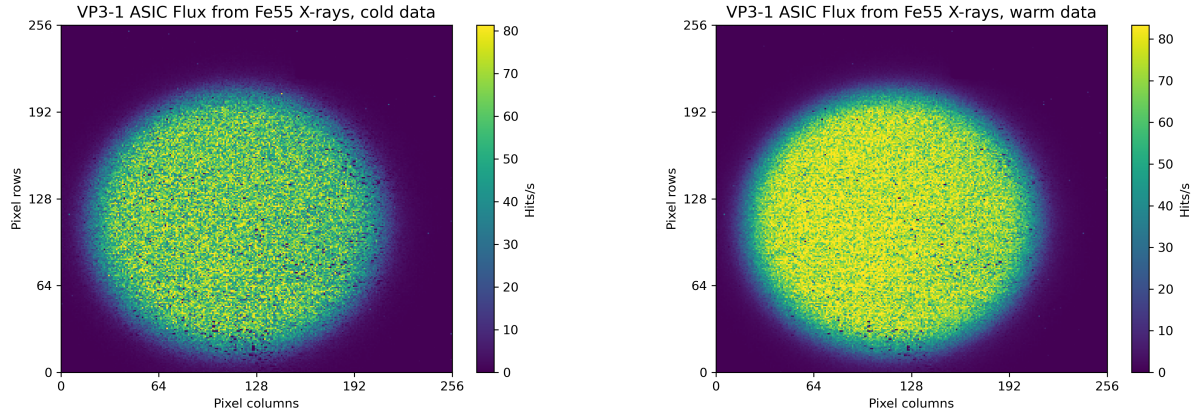

(a) Cold dataset.

(b) Warm dataset.

Figure 10: Total Flux summed over all thresholds for both the cold and warm dataset.

The datasets used, named *20230803_coldFe55* and *20230823_warmFe55*, were taken without displacing the ASIC from the radiation source, a factor relevant to test the influence of exposure time and module temperature. Future studies should control the ASIC position, together with other variables related to the setup, such that better assumptions can be made as well as possible extra tests on the data.

3.2 Data Filtering

The first step in the data processing is the removal of artefacts. These can be identified manually, directly inferred as sudden changes in the flux over threshold scan, and confirmed from the hit map that there was some issue with the data acquisition process. An example of this is shown in Fig. 11.

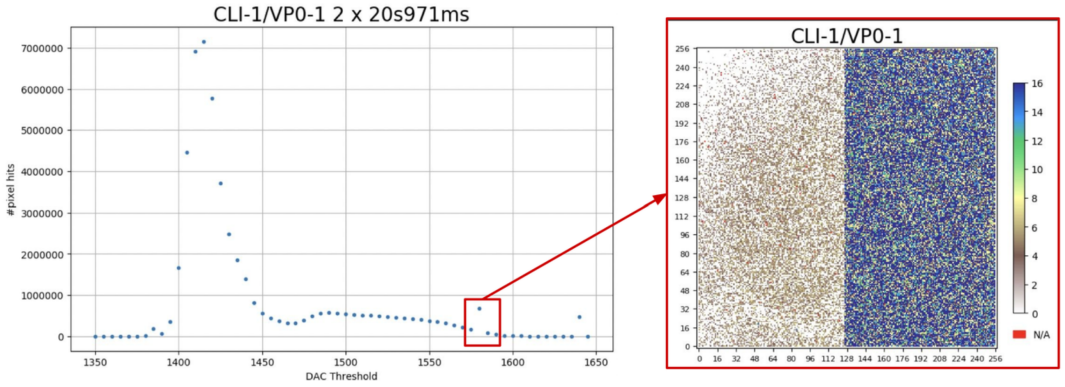

Figure 11: Noticeable anomalous flux data point observed in threshold scan. The ASIC and ST shown are different from that of the datasets used but shows what is referred to as a deviation in flux. Figure obtained from [12]

This problematic data acquisition issue was observed in the *warm* dataset here considered, shown in Fig. 12. After these anomalies in the data acquisition have been spotted, the specific problematic threshold and acquisition can be added to the dataset information so that these are not included before delving further into the data analysis.

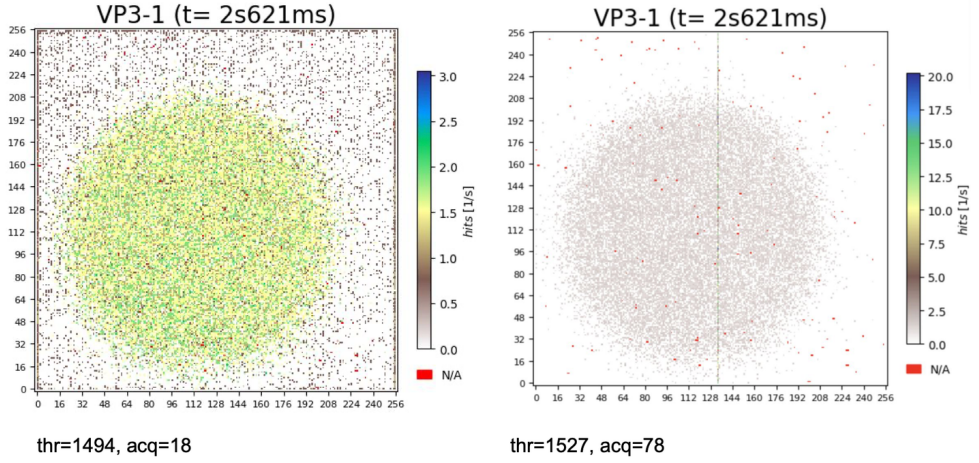

Figure 12: Outliers in flux measurements for VP3-1 ASIC in the *warm* dataset. Figure obtained from [13]

Raw data is further filtered by applying the mask matrix obtained from the equalisation procedure, thereby neglecting individual pixels that behave oddly. An extra check on the data is performed by looking for empty, bad and good scans:

- *Empty scans*: applies to the acquisitions where there are no hits. The mean of all the hits recorded at said acquisition is found, and then is compared to zero, using a tight tolerance of 10^{-9}. If *True*, skips the acquisition and does not consider it for the flux files.

- *Bad scans*: applies to the acquisitions where the data transfer from pixel to hard drive went wrong. Reason unknown. These acquisitions can be identified because the mean value of hits in the right-most last column are (approximately) 18.34 and 17.69 hits for the *warm* and *cold* dataset, respectively. These acquisitions are removed from their respective dataset.

- *Good scans*: applies to the acquisitions where none of the above conditions are met. The total number of good acquisitions per threshold is saved to be taken later into account for the computation of the flux.

After filtering the raw data, it is converted into flux files, which contain information on the flux for each individual pixel and for the whole ASIC over the threshold scan in which the measurements took place. The distinction between the overall ASIC and the individual pixels' flux is important, since it will become relevant when testing if it is possible to obtain accurate information about the gain of the individual pixels by just studying the ASIC flux, rather than performing the pixel by pixel analysis. This will be further discussed in Sec. 6.2.

3.3 Fitting and Pixel Categorisation

After the generation of the flux files for the individual pixels and for the ASIC as a whole, flux over the threshold scan data can be fitted to the flux equation 4. Pixels are classified based on a χ^2 test, which asserts the goodness of the fit based on the following equation:

$$\chi^2 = \sum_i \left(\frac{O_i - F_i}{U_i} \right)^2 , \tag{17}$$

where O is the observed flux, F is the calculated flux from the fitted parameters, and U is the uncertainty of the observed flux. This is essentially just comparing the observed value from raw data to the predictions from the flux equation.

With the parameters found from the fit to the flux data points and their associated uncertainties, one obtains the expected theoretical flux F. Thus, it becomes possible to obtain a value for the χ^2 of that pixel and compare it to some critical value χ^2_c. The χ^2_c is found using a confidence interval parameter of $\alpha = 0.05$ and the number of degrees of freedom is fixed to be the number of flux data points being analysed minus the constraints, these being the 4 fitted parameters A, E_0, f and s. However, the number of constraints might change when considering other flux equations, such as those considered in Sec. 2.1.2 later on. Based on this comparison, a pixel can be assigned with one of the 4 different labels below presented:

- *Good*: fit found for the individual pixel and passed χ^2 test.

- *Bad*: fit found for the individual pixel but not passed χ^2 test or unphysical parameters (negative values found for the flux equation parameters).

- *Fit Not Found*: fit not found for the individual pixel, since it could not converge when fitting data to the flux equation provided.

- *Cut data*: pixels that were cut due to masking, data anomalies, no hits recorded or other specific reasons.

However, for the sake of this analysis, we are only interested in the behaviour of the *good* pixels and in that of the whole ASIC, thus we will ignore the 3 other categories of pixels. After the data was processed, matrices containing the various parameters involved in the flux equation are saved, only considering *good* pixels. These can later be plotted as heatmaps, as shown in the Appendix B and throughout this study, to obtain a better understanding of the behaviour of the pixels and ASIC.

One extra point to be made is that, it is expected that the number of pixels categorised as *good* is not greatly influenced by the exposure time of the ASIC to the source, but rather to how well the data fits the flux equation, based on the above categorisation. Thus, it would be reasonable to assume that, when analysing the *cold* data, since there are fewer fluctuations within the pixels, this would lead to more physically precise data taking (referring to the DAC threshold at which the hits are recorded) leading to more pixels receiving the *good* category (since the model should describe better the flux behaviour). This assumption is tested in Sec. 4.2 and it is introduced here to be used as an argument later on.

3.4 Average behaviour of pixels: Mean, ASIC and ASICgood

There are various parameters that can be used to portray the overall behaviour of the 65.536 individual pixels. The first measure that comes to mind is of course the mean. This mean value for the various physical parameters gives a realistic representation of how the pixels behave on average from the measurements taken.

When the flux files are being generated from raw data, an average flux can be calculated by summing up the hits recorded by all the pixels over each threshold and dividing by the total number of pixels in the ASIC, i.e. 65.536. This average flux is what will be referred to as "ASIC" value. This average flux is fitted to the Eq. 4, also used by the individual pixels, and its physical parameters are carried throughout the analysis.

Another option to be explored regarding the ASIC value is to only consider those pixels categorised as *good*, which will be referred to as "ASICgood" value. This would essentially make the ASICgood parameter less biased from the true average than the original ASIC value due to the lack of contributions from other *bad* fit categories. Nevertheless, for the calculation of this new average flux, information on the category of each pixel is needed, which requires the individual pixel analysis to take place.

Performing the analysis on the ASIC flux is a computationally fast process, whereas carrying it out on all the individual pixels is more time-consuming, since the computation needs to be reiterated for 65.536 individual pixels. If it were possible to retrieve information about the gain of the individual pixels by exclusively looking at the ASIC flux, it would not be necessary to go over all pixels to have an understanding of their mean gain. This idea will be further explored by looking at the parameter distributions coming from the individual pixels together with the mean, ASIC and ASICgood, although the latter value requires the full analysis of individual pixels.

4 Analysis

4.1 Individual vs Average Flux

The flux over the threshold scan is shown below, with pink representing an individual pixel of choice and green the sum over all pixels, previously defined as ASIC in Sec. 3.4. Both flux curves have their respective fits using the flux equation Eq. 4 plotted.

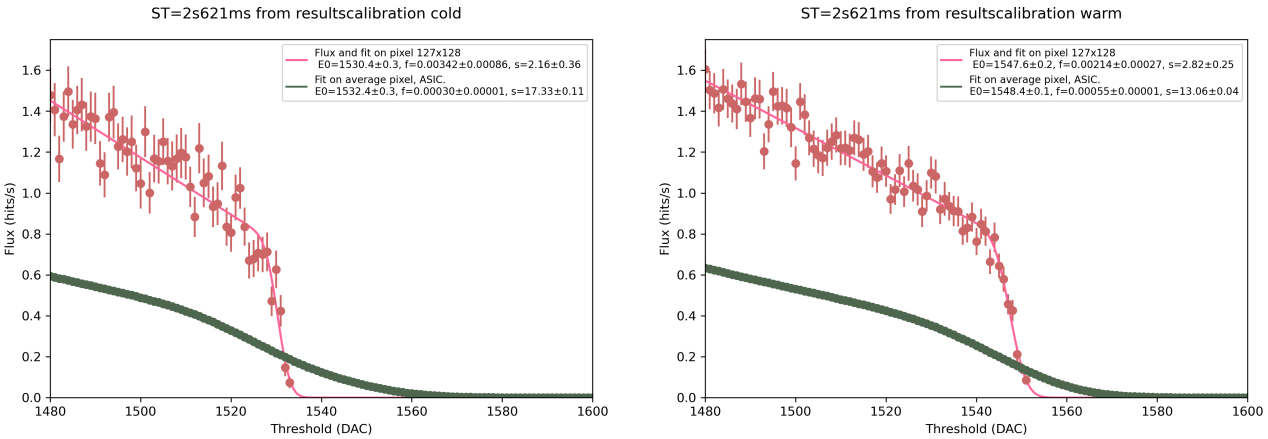

(a) Flux over threshold from the cold dataset.

(b) Flux over threshold from the warm dataset.

Figure 13: Comparison of the flux between the average (green) and individual pixel 127 x 128 (pink), for both the cold and warm dataset. The green/pink line correspond to the best fit of the flux model to the data.

The pixel chosen here is 127x128, which is located in the region with most exposure to the source, but any arbitrary pixel should exhibit similar flux curves, with slight differences coming from pixel to pixel variations. There are no significant dissimilitudes coming from the temperature difference regarding these fit curves, except for a major one, the E_0 location, but a more detailed comparison between *cold* and *warm* parameters is shown in Sec. 4.3. From the statements in Sec. 2.2, it is known that the pixels will have variability on the measured E_0 due to pixel-to-pixel variations, even though there should be an agreement on this value. The differences between various pixels regarding their flux curves are shown below for the *cold* and *warm* datasets.

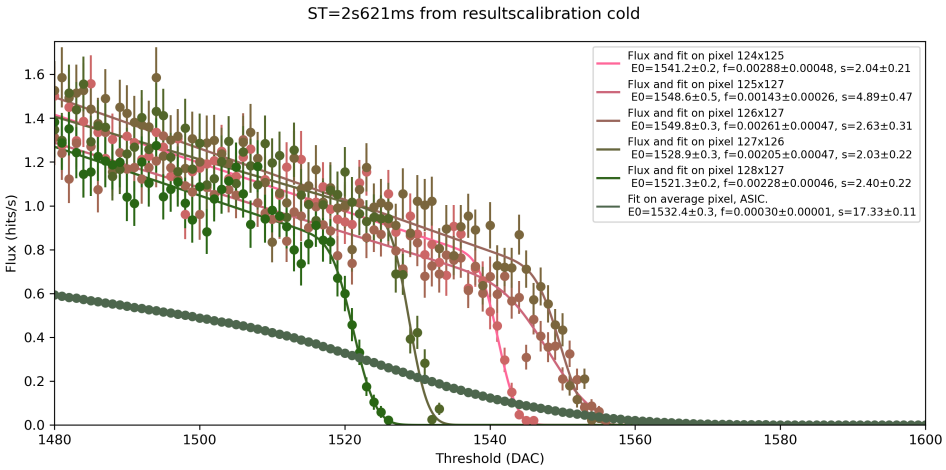

Figure 14: Flux curves over threshold scan for 5 different pixels, for the *cold* dataset.

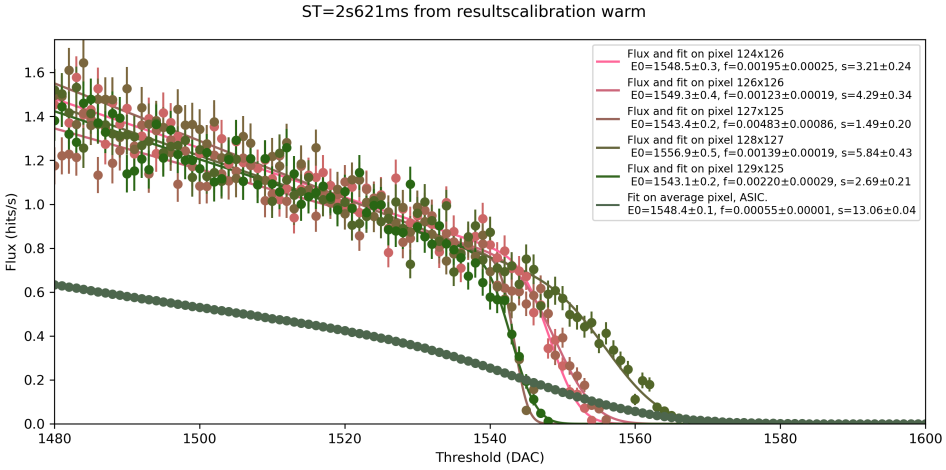

Figure 15: Flux curves over threshold scan for 5 different pixels, for the *warm* dataset.

There are various reasons that can explain the tendency of pixels to show higher DAC values for the drop in flux in *warm* data: increased thermal noise, increase of leakage current, extra phonon interactions and changes in charge trapping or in the depletion zones. Even though the agreement on the location of this flux drop would be the ideal scenario for this analysis, it is known that the detector presents pixel-to-pixel differences and it is designed to operate at lower temperatures. Thus, the *warm* data is showing the possible temperature influence on the data and not the true expected pixel characteristics, while the *cold* pixels do show the expected E_0 variation.

The ASIC flux does seem to slightly change from one dataset to another, mainly due to the already shown tendency of the pixels towards higher DAC values in the *warm* data, which can be seen from Figures 14 and 15. Additionally, aside from the E_0 variation, the s parameter also changes noticeably for some pixels, which accounts for the sharpness of the drop in flux. However, there are not many pixels that find a significantly higher s value, shown later in Sec. 4.3, therefore, the flatness of the ASIC flux curve comes from the obvious variability in the E_0 value from pixel-to-pixel, washing out the abrupt drop in flux.

4.1.1 Detailed Analysis on the Flux Equation: Residuals and Pulls

There is no proper derivation for the flux equation shown in Eq. 4, and it is taken to be a decently working model to fit the data. The residuals and pulls are computed, determining the goodness of the fit using the flux model to the data, which might provide insights on future improvements to this flux equation.

The residual r_{thr} provides a clear measure on how much the flux equation used deviates from the actual data points. The pulls are also calculated when the uncertainty related to the measured data points obtained was provided. The pull p_{thr} is the ratio between the residuals over the uncertainty, a measure of how far the model equation being fitted is from the recorded data. Both the residual and pull expressions can be seen below,

$$p_{thr} = \frac{r_{thr}}{\Delta F_{raw,thr}} = \frac{F_{raw,thr} - F_{fit,thr}}{\Delta F_{raw,thr}}$$

where $F_{raw,thr}$ and $\Delta F_{raw,thr}$ is the flux and its associated uncertainty obtained from raw data and $F_{fit,thr}$ comes from the fitted curve. The flux, residuals and pulls over the threshold range are shown below for the main/calibration flux model shown throughout this study, introduced as Eq. 4. The pulls are computed for the ASIC and ASICgood average flux curves, both for *warm* and *cold* datasets, as well as for a set of pixels from the centre of the Velopix to assess the accuracy of fit to the data of individual pixels.

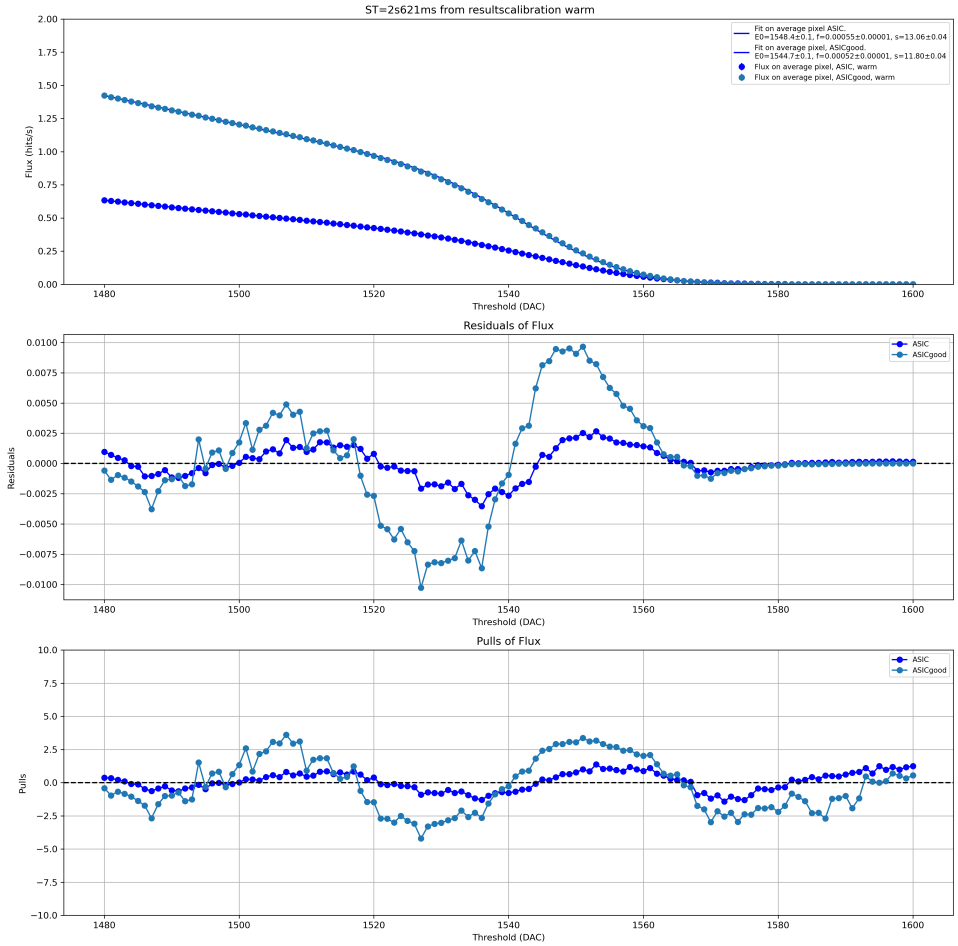

Figure 16: Flux, residuals and pulls for ASIC and ASICgood with warm data.

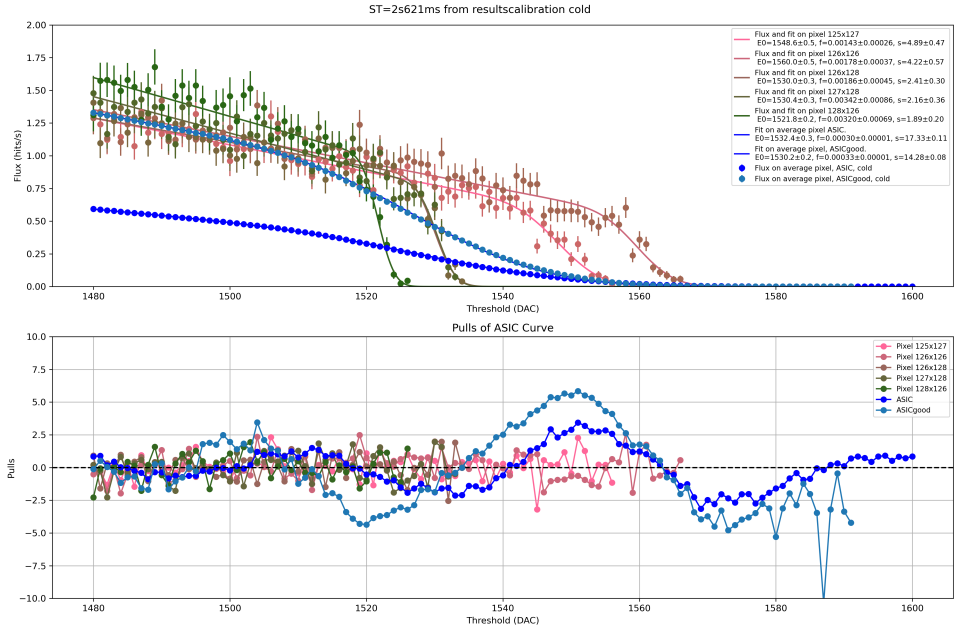

Figure 17: Flux and pulls for ASIC and ASICgood and some centre pixels with cold data.

Figure 16 gives a better overview of the failure of the flux equation to fit the data in some threshold regions, while in other locations the fit is decently close to the raw data points. The main concern coming from these plots is the fact that the model used does a worse job at fitting the ASICgood flux curve, which is intended to be a less biased measure of the average flux of the individual pixels, compared to the original ASIC curve considered. This can be concluded by looking at the residuals and the pulls of the ASIC curve being smaller than that of ASICgood.

Another issue that can be seen from comparing Figs. 16 and 17 is the fact that the *cold* ASIC and ASICgood pulls are greater than that of the *warm* dataset, with this feature being more prominent in the 1545-1560 DAC region. Considering that in the *cold* dataset it is expected to have more accurate data, this is an issue to be resolved since the opposite is observed from these subplots on the ASIC and ASICgood flux curves.

Since the ASICgood flux curve exhibits a greater amount of flux as well as a sharper drop, due to the contributions to this curve coming from only *good* pixels, it is certainly more similar in shape to the flux curves of individual pixels, which then raises the question of what the residuals and pulls will look like for the individual pixels. This is shown in Fig. 17, and it is easy to see that the individual pixels' pulls shown it is a decently good fit.

Therefore, one can conclude that since the fit of our flux equation performs decently well on the individual pixels, it is safe to use results coming from the mean of all the pixels considered, whereas the use of the ASIC and ASICgood values now become somewhat questionable, and suggest the need for improvements if one wants to have an accurate description of the overall ASIC flux.

4.2 Fitting to data

Performing the χ^2 test aforementioned gives a categorisation of the pixels, this being represented in the plots below:

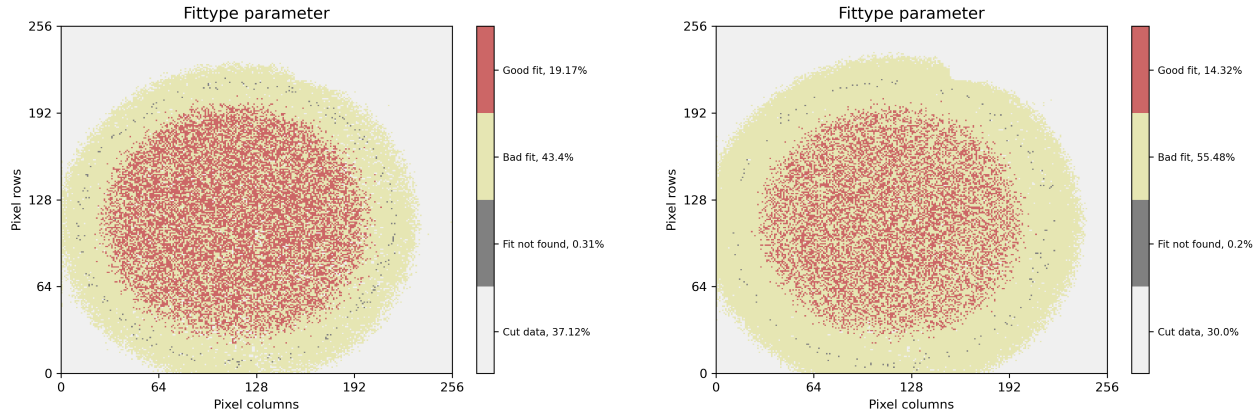

(a) Cold dataset.

(b) Warm dataset.

Figure 18: Heatmaps showing fit type category given to the individual pixels for the *cold* and *warm* dataset.

As it can be inferred from the heatmaps, there does not seem to be a great difference between the fit type heatmaps of the *cold* and *warm* datasets. However, there is a difference on the number of pixels that found a *good* fit, greater in the *cold* data. One finds 19.17% and 14.32% of *good* pixels with respect to the total number of pixels of the ASIC, for the *cold* and *warm* datasets respectively.

The assumption stated in Sec. 3.3, expecting a higher number of *good* pixels from the *cold* data due to its more physically accurate measurements with less thermal fluctuations involved within the pixels, can now be tested. This is supported by observation of the exposure time difference in Table 2, with *warm* data having almost twice as much as the *cold*, while the latter finds a greater number of *good* pixels. Hence, a greater exposure time is correlated with more *good* pixels, but not strongly. Thus, it can be argued that the main influencing factor for finding *good* pixels is the Module temperature. To fully test this assumption, it would have to be proven

that the variation of the exposure time of the ASIC to the radiation source does indeed not greatly influence the amount of pixels classified as *good*, which is confirmed in Sec.5.1.

Furthermore, we see a circular distribution of the fit categories, with its centre being the point where the source was located and from where the pixels will start to receive less radiation moving radially outwards. The plot can be broken down into four different sub-circles, corresponding to *good*, *bad*, *fit not found* and *cut* pixels. The pixels categorised as *fit not found* exhibit this circular pattern, but with a specific radial location and with a ring-like structure. This is briefly explored in Appendix C.

The results on the gain coming from this study will depend on the flux equation used and their behaviour when used as models to fit the data. Therefore, it becomes important to test the other possible flux equation variations shown in Sec. 2.1.2 to find the most appropriate candidate, from which the in depth analysis will be performed.

4.2.1 Testing various flux models

The same analysis as for the original flux equation and *calibration* approach was performed, using the flux equations defined in Sec. 2.1.2, and the amount of good pixels found for both *cold* and *warm* datasets are shown below.

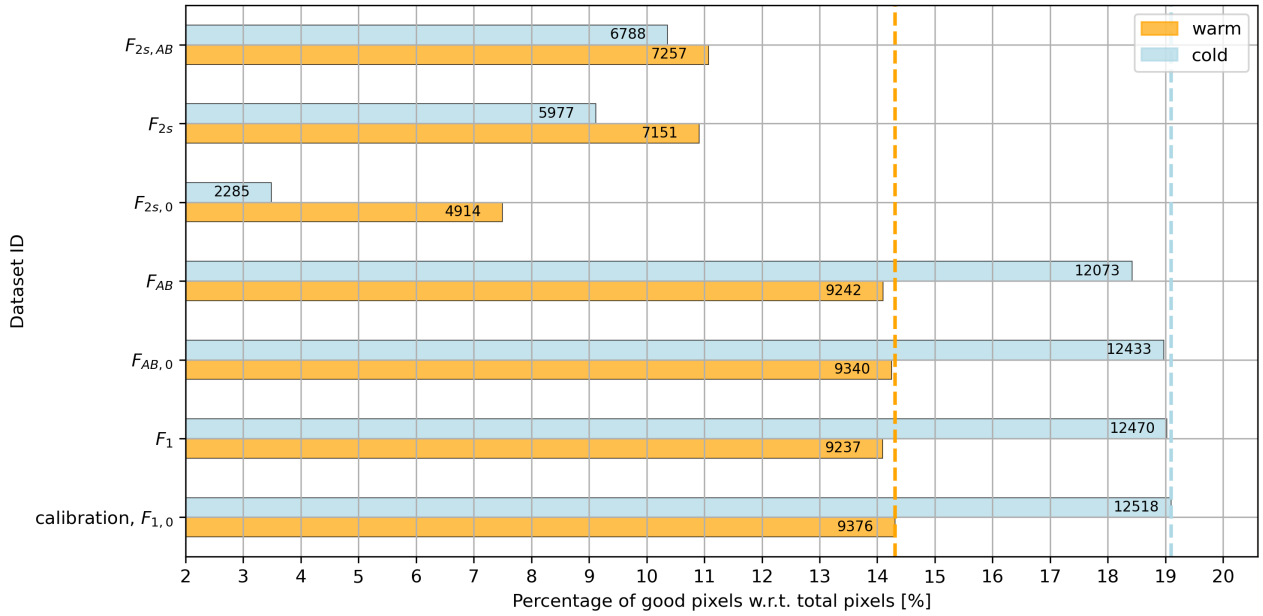

Figure 19: Summary of percentages of *good* pixels found for variations to the flux equation. The specific number of *good* pixels found is shown within its corresponding bar.

First, comparing the original flux equation $F_{1,0}$ to $F_{AB,0}$, it shows that the inclusion of A^* and B^* as two independent scaling factors does not seem to influence much the amount of *good* pixels found. Of course, in the original flux equation, the A and f parameter can also freely vary to fit the data better but not as independently of each other since the terms are governed by them. This essentially shows that, even though one would think that having the terms in the flux equation being independent of each other would lead to more freedom while fitting the data and thus find more *good* pixels, the $F_{1,0}$ using A and f, with the individual terms involved being more constrained by their related scaling factors Af and $A(1-f)$, seem to provide slightly more *good* pixels. From this, it is shown that the two models are equivalent parametrisations, which is not obvious yet expected, and that one can assume that the various terms in the flux equation should be directly related, such as in $F_{1,0}$ in the *calibration* approach.

When comparing the original flux equation to $F_{AB,0}$ and F_{AB}, with and without including the term0 respectively, they seem to be finding approximately the same percentage of *good* pixels with respect to $F_{1,0}$ or F_1, with

the *cold* dataset consistently finding more good pixels than that of the *warm* dataset, which is an anticipated but expected feature explored in Sec. 5.1. From the differences between the functions which include the term0 or not, it can be inferred that its inclusion in the flux equation is reflected in a minimal increase of *good* pixels, which will only make a deviation in the mean gain of the datasets in the decimal places, so the explicit contribution of this term0 is very small and only contributes to a possible better understanding of the flux equation.

Secondly, F_{2s} and $F_{2s,0}$ seem to find a number of *good* pixels which differs greatly to that of *calibration*, together with the fact that they are inconsistent with the reasonably established feature that there should be more *good* pixels found in the *cold* rather than in the *warm* dataset. These generalisations of the flux model F_1 should be describing the data as equally well as their original counterparts. Nevertheless, this is not observed in the amount of *good* pixels and, for the aforementioned reasons, it is safe to conclude that flux equations that involve two s parameters, s_1 and s_2, such as those presented as $F_{2s,0}$, F_{2s}, $F_{2s,AB}$ in Eqs. 10, 11, 12, are not adequate models to represent the datasets, at least with the equation structure used. It might be that an improved flux equation with 2 s parameters describes the data well, nevertheless, it presents issues finding a fit, due to failure of convergence due to the extra degree of freedom, taken into account in the χ^2 test.

The last flux model in Sec. 2.1.2, shown in Eq. 13, was used but not included in the results above. This flux model did not provide any insights since it has trouble converging to a fit due to other possible reparametrisations which will give identical solutions (e.g. $f \to 2f, A \to \frac{A}{2}, B \to B \cdot \frac{1-f}{1-2f}$). It is left as a remark for future exploration of models to describe the flux data.

The main conclusion obtained from testing the different flux models is that the main flux equation, $F_{1,0}$ shown in Eq.4, performs best compared to its variations, finding a greater quantity of *good* pixels while not having too many free parameters involved, leaving the model highly constrained.

4.3 Parameter Analysis

The following distributions for *good* pixels were found using the main flux model Eq. (4), showing the parameters E_0, f and s which determine the flux equation, both for the *cold* and *warm* dataset respectively. Note that the error given with the mean values found is the $SEM = \sigma/\sqrt{n}$, while the errors of the ASIC values are obtained from the fit of the flux curve directly.

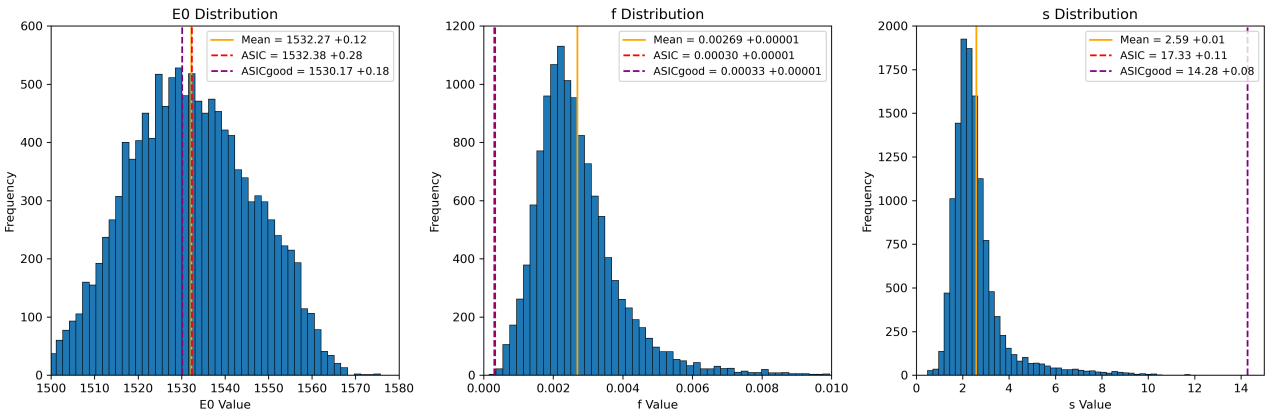

Figure 20: Cold dataset parameter distributions showing the mean, ASIC and ASICgood values.

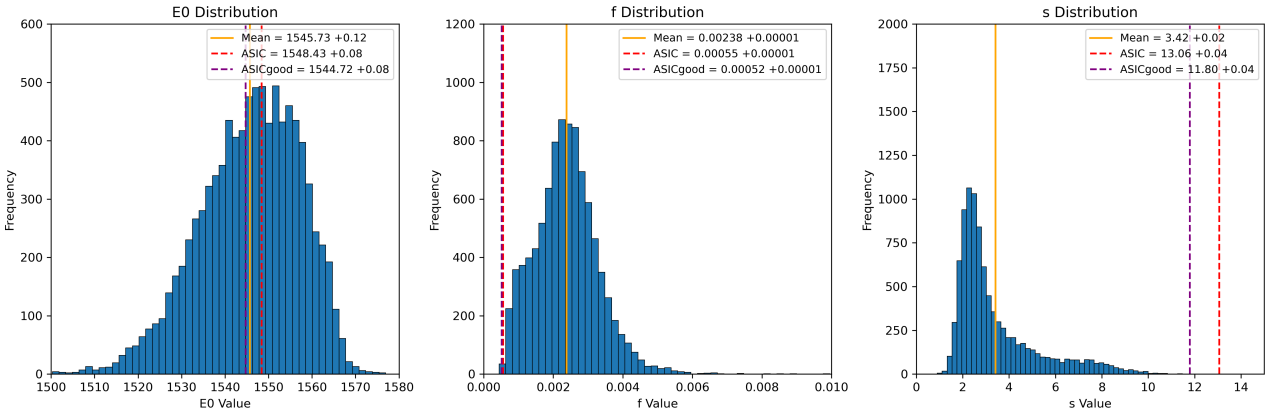

Figure 21: Warm dataset parameter distributions showing the mean, ASIC and ASICgood values.

Looking at the three histograms and comparing the found mean, ASIC and ASICgood values, it is clear that, even though in the E_0 distribution all of these vertical lines lie close to each other and seem to be almost consistent on a value, there is a clear disagreement on the f and s mean and the ASIC or ASICgood values. This is due to the differences in behaviour between the individual and the average flux, which have a somewhat distinct flux to threshold curve, a dissimilarity already portrayed in Fig. 13, specially on the s parameter, associated with the sharpness of the drop in flux.

The distributions of the f charge sharing parameter revealed similar distributions for both datasets, with some pixels finding smaller f values in the *warm* dataset, slightly lowering the mean f. Looking into the drop in flux using its associated parameter s, the mean found by both datasets are close to each other, but with a higher value on the *warm* dataset. This comes from some pixels finding a higher s parameter, associated with the tendency of flux data points towards higher DAC values due to Module Temperature influence, which can lead to widening in the flux drop, explained in Sec. 4.1.

The shape of the distributions is very similar between *cold* and *warm* data, however, the E_0 distribution does present a prominent change. It becomes obvious that the *warm* dataset finds a more skewed distribution than that of the *cold* data, linked to the shift in E_0 towards higher DAC values due to Module temperature influence. From this, it is certain that the dataset which will provide more physically accurate results is the *cold* dataset, due to its greater amount of *good* pixels and the resemblance of the E_0 distribution to that of a Gaussian, as expected from the Central Limit Theorem for an energy deposition measurement. Nevertheless, a much smaller spread on the E_0 distribution is expected from a quasi-monochromatic source of radiation, suggesting a possible bias and need for correction to have a more reliable determination of the energy deposition.

4.4 Parameter heatmaps and E_0

The parameters found for the *good* pixels can be also represented as a heatmap distribution over the ASIC, which might reveal some information on the spatial pattern of these values. If there were to be any discernible structure in the spatial distribution, it would imply that there exist local biases in the detector, which would not be suitable for its operation. Nonetheless, this scenario is not expected since the ASICs undergo careful inspection during the production process.

The heatmaps for the parameters involved in the flux equation are shown in Appendix B. All of them are just randomly distributed values over the detector, with only minor variations in the parameter values from pixel to pixel. The only somewhat relevant heatmap to be shown in this subsection would be the difference between the individual E_0 values and the found E_{0ASIC} value, since, if there were to be any observable pattern, it would suggest that there might be a systematic uncertainty related to the position of the pixel.

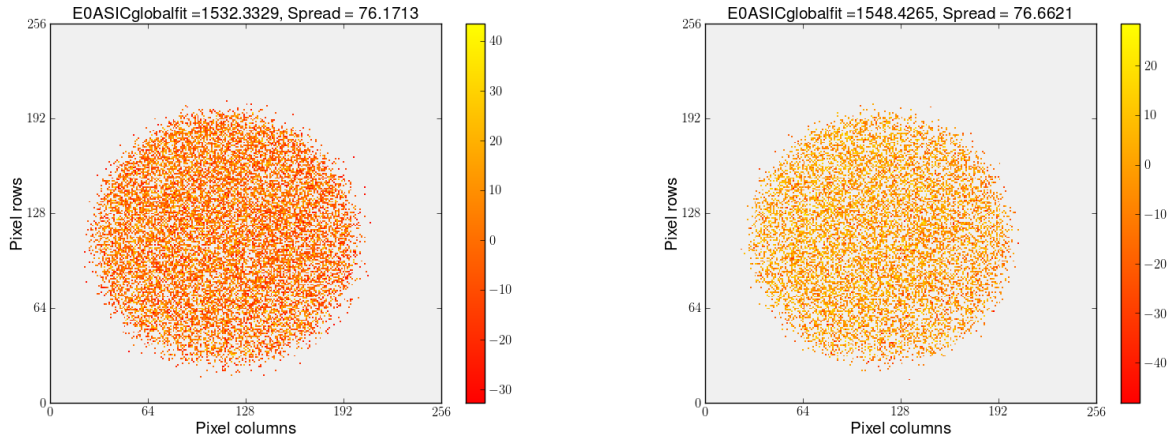

(a) Cold dataset.

(b) Warm dataset.

Figure 22: Difference heatmap between E_0 and E_{0ASIC} for both cold and warm datasets. The spread shown in the top of the graph refers to the difference between the maximum and minimum difference value.

From the above figures, there is not any noticeable structure observed, meaning that there is no correlation between the pixel coordinate and their value of E_0. Nevertheless, this topic is further explored in Sec. 5.2.

In order to explore in a quantifiable manner how far each pixel lies from the ASIC, a z-score test can be applied, that is,

$$z = \frac{x - y}{\Delta z}, \text{ with } \Delta z = \sqrt{\Delta x^2 + \Delta y^2} \tag{18}$$

where $E_0 = x \pm \Delta x$ and $E_{0ASIC} = y \pm \Delta y$, and the result being the closeness of the pixel value to E_{0ASIC} in number of standard deviations σ. The found distributions are shown below:

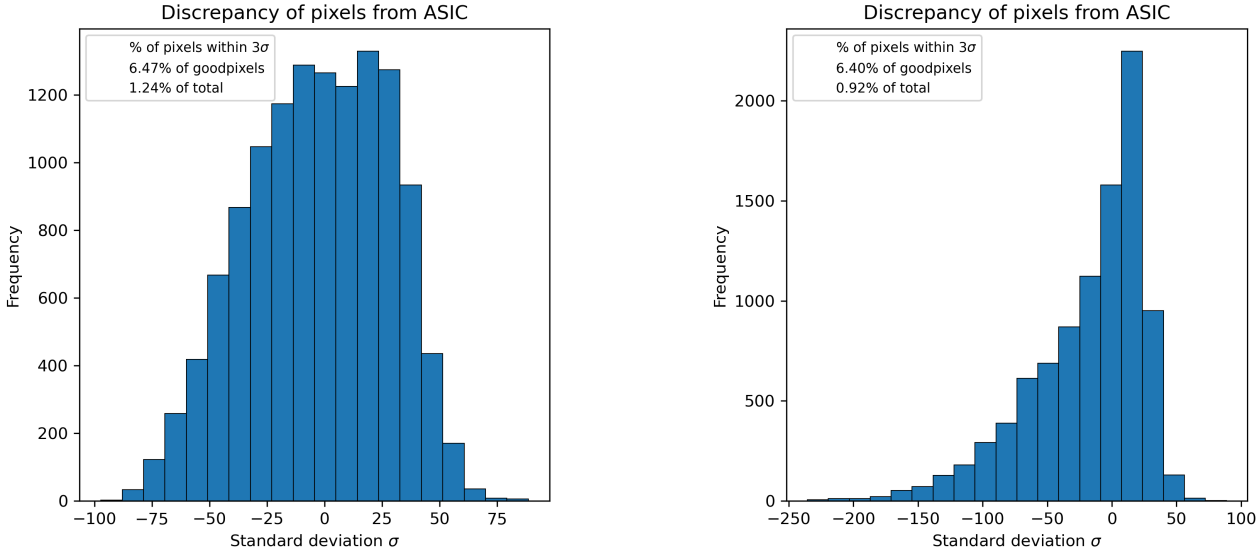

(a) Cold dataset.

(b) Warm dataset.

Figure 23: Discrepancy of E_0 between the pixel and E_{0ASIC} in number of standard deviations. The legend shows the percentage of pixels within 3σ of the ASIC value, compared to good and the total amount of pixels. Note the difference in scale of the x and y axis between the figures.

From this, it can be inferred that the found value of E_{0ASIC} is not so representative of the individual E_0 values from the pixels when taking into account their uncertainty. The spread in number of standard deviations σ,

as it can be seen from the x-axis range, is extremely large, with pixels deviating more than a 100σ from E_{0ASIC}.

From the parameter distributions shown in Fig. 20, it was already anticipated that there might be a bias to correct for, since there is a big spread found on the E_0 distribution, while a narrower distribution is expected from a quasi-monochromatic source of radiation. This previous observation together with these two extra plots show that it is wiser to look for another parameter which will have a better representation of individual pixel values when comparing them to the average/ASIC. The next obvious parameter to do so would be the target E_t, due to the inclusion of the noise baseline E_b correction to the E_0 values.

4.5 Target E_t and E_{tASIC}

In this section, the introduction of the noise baseline shift is explored. Its implementation allows for an energy deposition measurement in DAC units and the correction for biases that arise from pixel variations, as explained in Sec. 2.2. The individual value of E_b for each pixel can be obtained from two approaches.

One option is to extract it from the location of the high peak in flux located around 1400 DAC, as shown in Fig. 6, corresponding to the noise baseline position. However, these threshold scan regions are not part of the datasets shown in Table 2, but are rather from two other datasets not included in this analysis. Since there could be influences from the predicted location of the maximum in the flux distribution, such as exposure time influence or assuming that the model and fit are correct in said region, this approach is not taken. A threshold scan with better resolution in the noise domain, as well as having a single scan covering both the noise and source regions would be best for this approach, given that the best flux model used to fit the data is found.

The second and most practical choice is to obtain it from the best Trim choice that results from the equalisation process, briefly introduced in Sec. 2.2. Since one of the main purposes of equalisation process is to accurately study and find E_b, it was the approach taken and thus the best Trim setting for each pixel, is used. The predicted Trim value can be off by 1 in the MiniDAQ2 equalisation, but the prediction from MiniDAQ3 should be slightly more reliable. The baseline for the whole ASIC is chosen to be the mean of the baselines of all pixels $E_{bASIC} = \overline{E_{b;i,j}}$, such that $E_{tASIC} = E_{0ASIC} - E_{bASIC}$.

Finding the value of E_0 from the fit to the flux curve and then shifting by the baseline E_b is mathematically equivalent to subtracting the DAC position of all the flux data points by the baseline and then performing the fit, from which the target E_t is determined right away. This allows us to obtain the error associated to the individual pixels and for the ASIC values without having to perform error propagation. The found target E_t distributions are shown below:

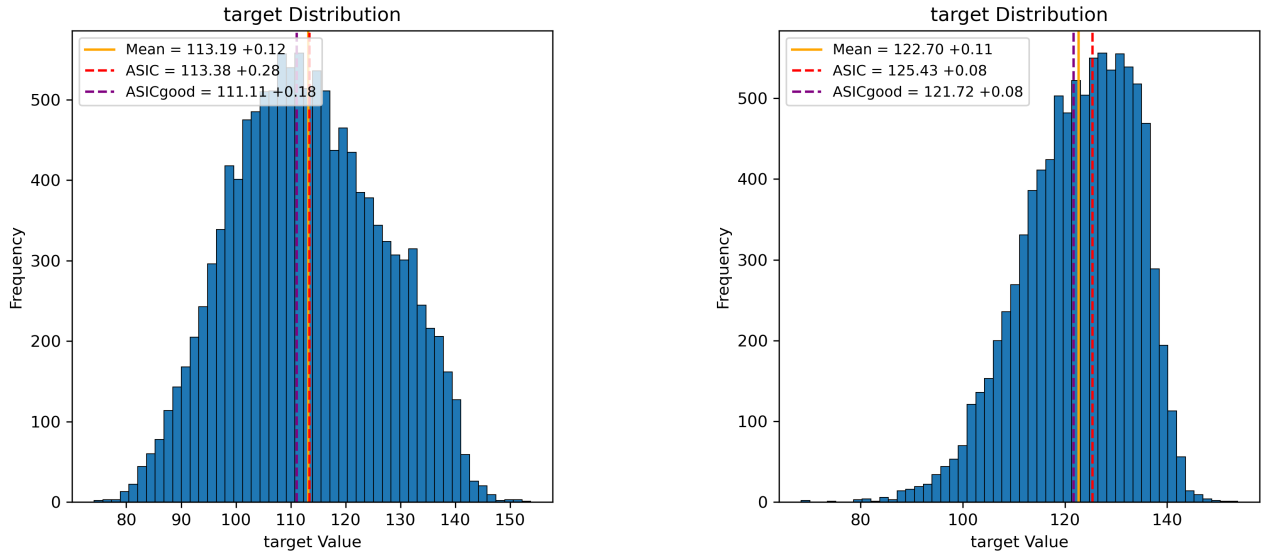

(a) Cold dataset.

(b) Warm dataset.

Figure 24: Target E_t distributions showing mean, ASIC and ASICgood value.

A z-score test such as that shown in Eq. 18 is used, but now being applied to the target E_t. This allows to determine how close a set value of x is to E_{tASIC} in terms of standard deviations σ. The individual and ASIC target uncertainties are obtained from the fit to the flux data points. The found discrepancy distributions are shown below:

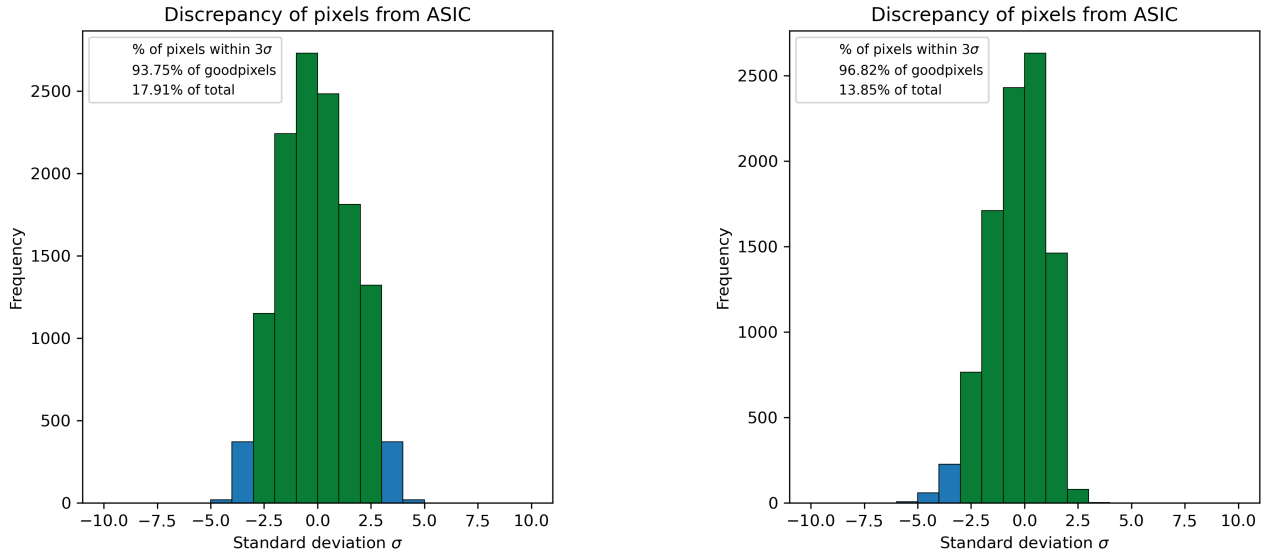

(a) Cold dataset.

(b) Warm dataset.

Figure 25: Discrepancy of E_t between the pixel and E_{tASIC} in number of standard deviations.

There has been a significant improvement on the representation of E_{tASIC} with respect to the individual E_t when comparing it to the discrepancy distribution of the E_0 show in Fig. 23. There are now 93.75% and 96.82% of *good* pixels within the 3σ range, for the *cold* and *warm* dataset respectively. The distributions are closer to the 99.7% representation expected from a Gaussian distribution.

4.6 From Target E_t [DAC] to Gain K[e-/DAC]

The target E_t can be used to obtain the conversion factor or gain K[e-/DAC] using Eq.15. From this equation, it is obvious that the gain and the target are inversely related up to some proportionality constant. Nevertheless, both the target and the gain are shown in the plot below for the *cold* and *warm* dataset.

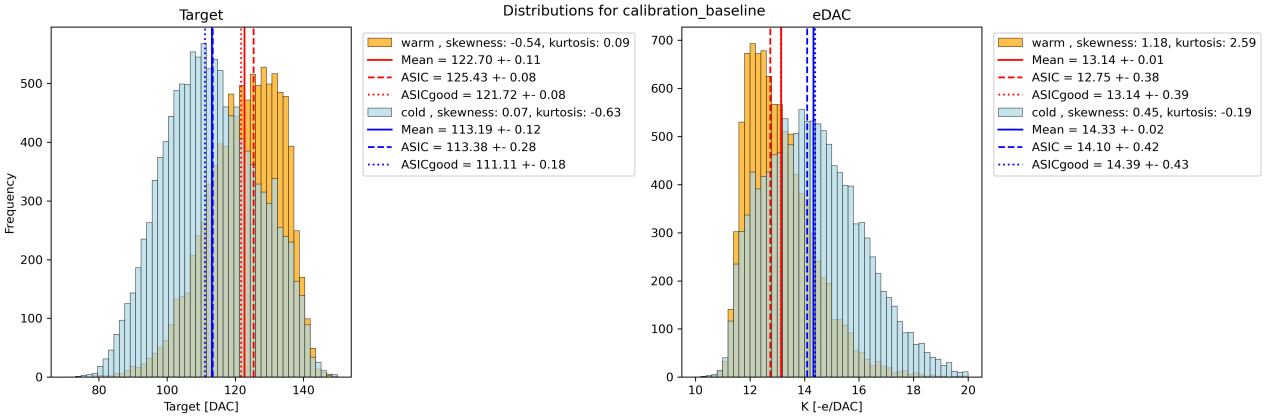

Figure 26: Summary of target and K distributions. The mean and error of the mean shown in plot and legend. The ASIC and ASICgood values and uncertainties obtained from fit to the flux curves.

Here are plotted the mean and its uncertainty, the error of the mean, calculated as $\sigma/\sqrt{n}$, with n being the

number of *good* pixels considered in the distribution.

First looking at the target distribution, it is obvious from the plot that the *cold* dataset tends towards a lower DAC value than that of the warm data, this again being most likely due to less thermal influence on the measurements. This can be further confirmed by noticing that the *warm* distribution is more asymmetric, rather than presenting an overall shift by some constant with respect to the *cold* data. Such an assumption can also be confirmed by looking at the higher DAC extreme of the *cold* and *warm* distributions, which they seem to agree on. This can quite possibly be explained by the temperature influence, which introduces extra phonons appearing in *warm* data and therefore, those hits which would have been recorded at a lower DAC value are shifted towards higher DACs.

If the mean and ASIC values disagree while taking into account the uncertainties associated with them, it would imply that the mean pixel would differ in gain K[e-/DAC] to that of the found value from the ASIC average curve, which implies that we cannot say anything about the gain of the individual pixels by exclusively performing an analysis on the overall ASIC data. Since the ASICgood flux curve still relies on the individual analysis and categorisation of the pixels, it cannot provide further insights on this topic but rather it represents another measure describing the average pixel and hopefully contribute for a better understanding on the flux of the ASIC and the pixels.

4.7 Performance

From the analysis developed in the next section, studies on irradiations of ASICs can be conducted to further explore their characteristics, including the characterization of their gain K[e-/DAC]. This would enable a better understanding of the differences between ASICs and their respective gain from real measurements.

The analysis shown analyses 1.71 rows/s on average and takes approximately 8 minutes to go over the entire ASIC using the best flux model chosen. The analysis time is given on average since there are rows containing more masked pixels or cut data, which take less time to analyse.

This makes the analysis on all pixels feasible, as it is not overly time-consuming, and it allows examining the pixel variations closely. However, choosing other flux models or other approaches might lead to longer data processing time if one has to go pixel by pixel, making the ASIC average value introduced in Sec. 3.4 a possible reliable and efficient choice instead of performing the analysis on all pixels. Nevertheless, this is only a plausible scenario if the ASIC gain value does make a suitable prediction of the mean gain, which is explored at the end of this study.

5 Systematic uncertainties and biases

An overview of the various steps and assumptions made throughout the data processing has been given in the above sections, as well as some early results on the statistical behaviour of the parameters involved. The approach used so far, this referring to the flux equation as well as other data specifics, will be referred to as *calibration*. The topics here presented explore the exposure time influence on the results and impact of pixel separation in different groups on the gain.

5.1 Exposure time influence

One of the main reasons to explore exposure time variation on the datasets, is to see its effects on the pixel categorisation. If the *cold* and *warm* datasets were to have the same exposure time, it would be possible to verify the reasonable assumption of temperature influence in the quality of data and pixel categorisation, rather than assuming that it is mainly the amount of exposure time to the radiation source what determines the percentage of *good* pixels, as mentioned in Sec. 3.3.

It was made clear in Table 2 that the *warm* dataset received more exposure time to the radiation source compared to the *cold* data. More explicitly, following from Eq. 16, it received twice as much exposure than the *cold* dataset,

$$\frac{t_{warm}}{t_{cold}} = \frac{nacq_{warm}}{nacq_{cold}} = \frac{100}{50} = 2 \implies t_{warm} = 2 \cdot t_{cold}$$

To test the influence of exposure time on the results, the number of acquisitions considered for each dataset was modified. The various modifications to the datasets and their code names for the results are listed below:

- calibration: original approach considering the *nacq* shown in Table 2. Both datasets have different exposure time t, with *warm* dataset having twice as much.

- calibration_nacq50: same as calibration, but using acquisitions in the [0,50] range. Both *warm* and *cold* datasets have equal exposure time t.

- calibration_acq0to25: same as calibration_nacq50, but using acquisitions in the [0,25] range. Both *warm* and *cold* datasets have equal exposure time t.

- calibration_acq25to50: same as calibration_nacq50, but using acquisitions in the [25,50] range. Both *warm* and *cold* datasets have equal exposure time t.

Using all these variations of the *calibration* datasets, it is possible to test the effects of exposure time difference on the results of this analysis. Note that a comparison between *cold* and *warm* data is only possible knowing that the overall position of the ASIC to the radiation source is the same in both datasets, as clarified in Sec. 3.1. The following results were obtained for the gain $K[e-/DAC]$ and the amount of *good* pixels, shown in the figures below.

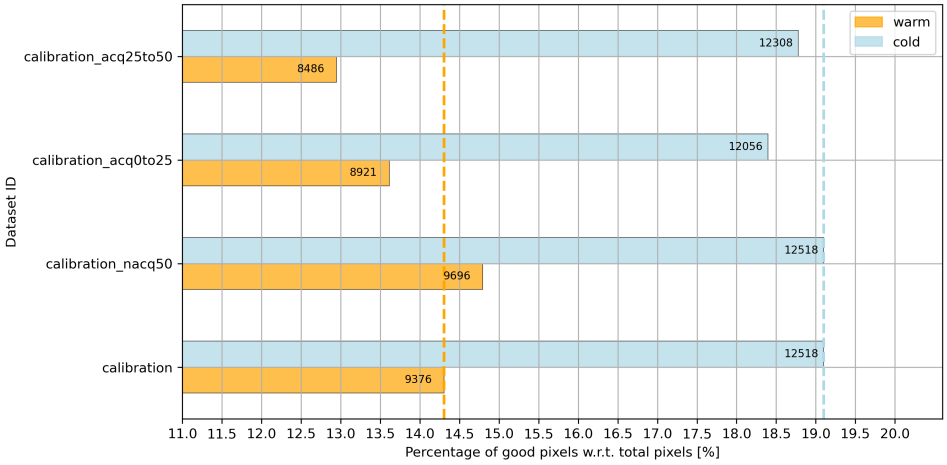

Figure 27: Summary of percentages of *good* pixels found for variations in exposure time, using the *calibration* dataset as reference for the different acquisition ranges considered. The specific number of *good* pixels found is shown within its corresponding bar.

Looking at Fig. 27, it is easy to see the influence of exposure time on the data quality. First, doing a comparison of the *calibration* datasets, where they differ in exposure time t, to the *calibration_nacq50* variant, where both datasets have equal t, it is clear that the *warm* dataset having twice as much exposure time in *calibration* made a difference. While the amount of *good* pixels remains the same in the *cold* data (since its number of acquisition was not changed), in the *warm* data, we see an increase of *good* pixels with the reduction of exposure time, which is not immediately expected, making this an observation worth exploring.

Now comparing *calibration* to the other variations (which contain less exposure time), more explicitly looking at the *warm* data, one can see the high difference in the amount of pixels categorised as *good*. While this difference in the number of *good* pixels also occurs in the *cold* data, there is certainly less variability. The high variation only present in *warm* exposures points towards the temperature having an effect on the quality of data, referring to how physically accurate the measurements on energy deposition are.

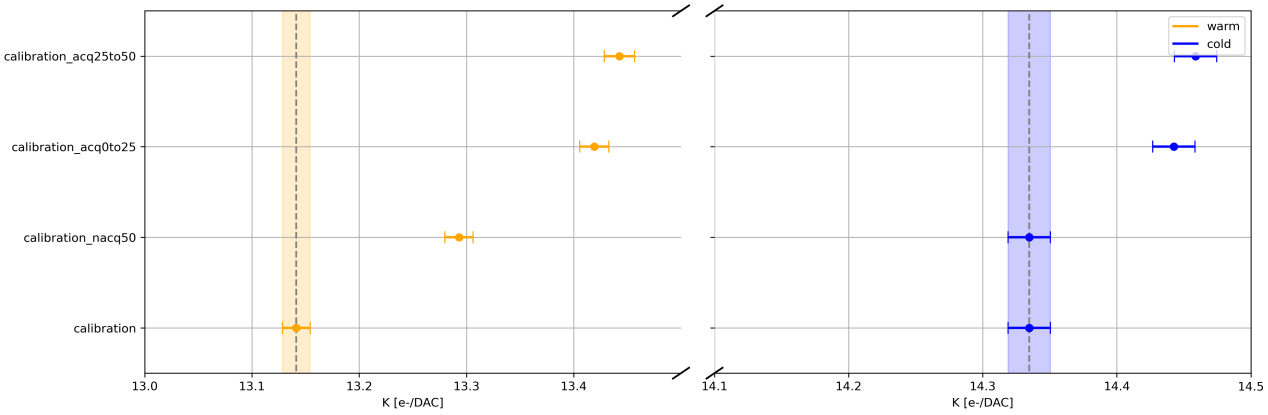

Figure 28: Summary of gain $K[e-/DAC]$ mean values for variations in exposure time, using the *calibration* dataset as reference for the different acquisition ranges considered.

In the figure above, the mean gain for each exposure time variation dataset considered is presented. Considering the *cold* and *warm* data separately, and explicitly comparing calibration_acq0to25 and calibration_acq25to50, it is not difficult to verify that the mean gains agree within their uncertainties, which is expected from a statistical process such as the irradiation here performed, since both of them contain the same exposure time but in different acquisitions. From comparison with calibration_nacq50, the inclusion of more exposure time does influence the amount of *good* pixels found and thus the mean gain K.

For the above reasons, it is fair to conclude that, although the exposure time of the ASIC to the source does influence the number of pixels categorised as *good*, it is the temperature related effects mainly influencing the quality of data acquisition. The inclusion of greater exposure time on the *warm* dataset most certainly lead to better data quality, since more hits coming from the incident particles can be recorded, which then lead to higher chance for the flux model to find a *good* fit, while for the *cold* dataset, less exposure time would have lead to similar quality of data, as shown in Fig. 27, but still making a difference on the mean gain value found.

Performing this study again with datasets of greater exposure time would lead to smaller differences on their mean gains, as observed in the *warm* data from Fig. 28, and eventually to a convergence to the true mean gain value both for *cold* and *warm* data. The study here presented takes into account the maximum exposure time available, which should provide the most accurate determination of the gain K[e-/DAC] possible.

From the differences calculated between the mean gain of the exposure time variation datasets with respect to the main/calibration value, a systematic uncertainty can be assigned to account for the exposure time influence. The systematic uncertainty is calculated using quadrature, obtaining $\pm$ 0.16 and $\pm$ 0.44 [e-/DAC] for the *cold* and *warm* dataset respectively. These are included with the final results in Table 6.1 and in Figure 33 as a gray band next to the error of the mean.

5.2 Groups of pixels: even, odd and 16th rows

During the equalisation process run on the real VELO, it was noticed that different groups of pixels behave slightly different from each other when it comes to the noise width [11]. This effect is said to arise due to the simultaneous firing of all pixels in the ASIC when the equalisation takes place, however, this is not the case when taking data such as the exposure to a radiation source, since only individual pixels are hit by the incident particles with a small charge sharing component to neighbouring pixels. Nevertheless, this fact can be cross-checked with the data taken for this study.

In order to do so, pixels are grouped in the same categories as in the equalisation study aforementioned, that being a separation of even and odd columns as well as a group containing data from every 16th row in the ASIC.The even and odd groups of pixels are mutually exclusive, while the 16th rows is not. One obvious remark that needs to be made is the fact that there are more pixels to be considered in the even/odd group than in the 16th rows category, and this will be reflected in the histograms and other measures such as the error associated to the mean. The analysis shown so far throughout this study is performed for the 3 groups, with the histogram for target and gain presented below.

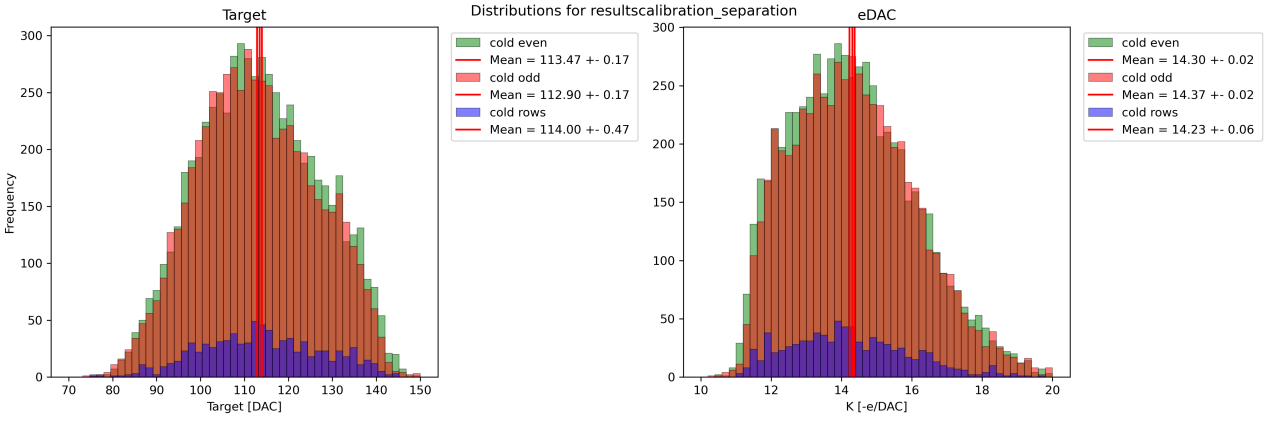

Figure 29: Target[DAC] and gain K[e-/DAC] histograms for *cold* dataset using calibration approach including pixel separation in groups: even, odd and 16th rows. The mean and its associated error for each group is shown underneath the colour label in the legend.

The above figure only shows the found distributions for the *cold* dataset, however, the *warm* dataset looks very much alike, differing slightly in shape as previously seen in Fig. 26. In order to see the differences between the even and odd group, it is possible to normalise the distributions by dividing the counts over the amount of

pixels of its corresponding group. The distributions below show the normalised difference in counts within each bin between the *even* and *odd* group for the target and gain of the *cold* and *warm* dataset.

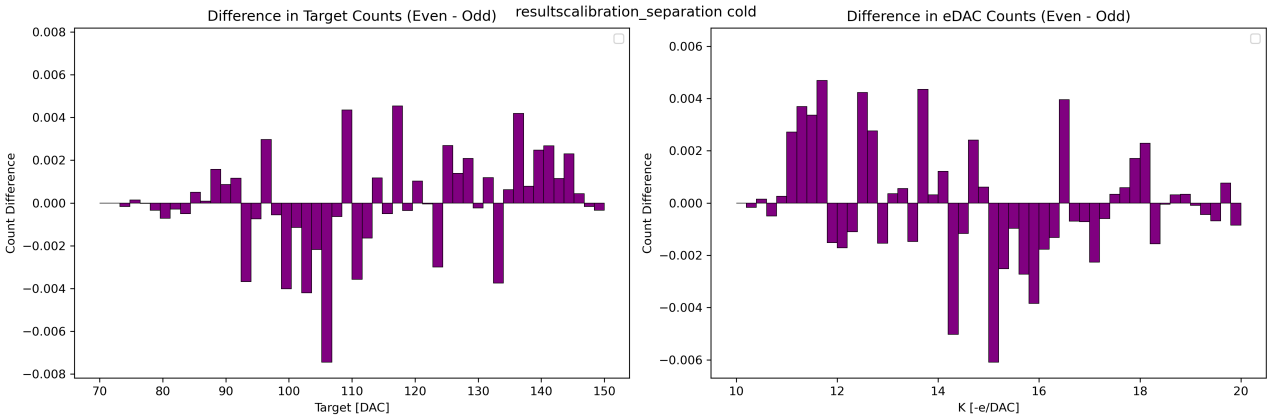

Figure 30: Normalised difference in counts between even and odd group for target and gain of the *cold* dataset.

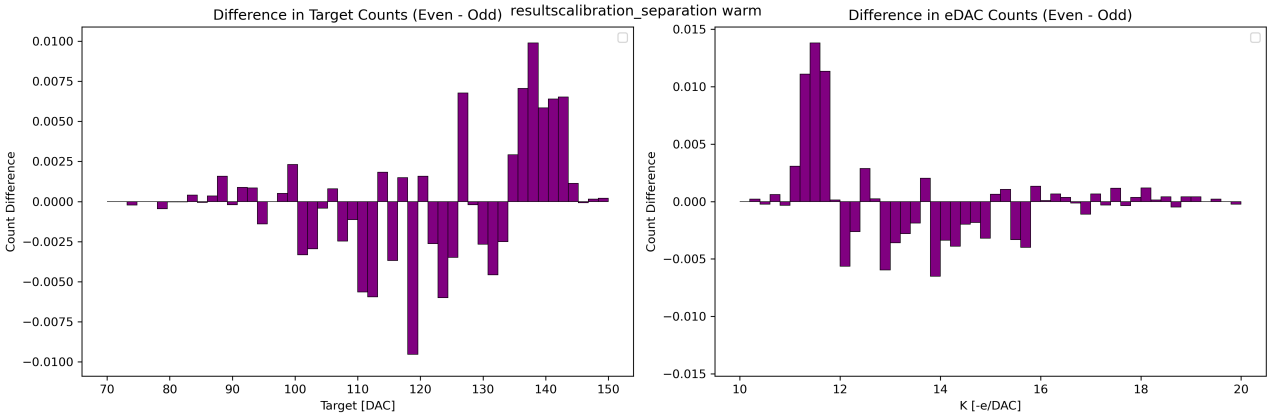

Figure 31: Normalised difference in counts between even and odd group for target and gain of the *warm* dataset.

The *even* group tends to find lower values for the gain, while the *odd* group tends towards higher gain values, an effect visible in both *cold* and *warm* data. Looking at the mean gain from each group, it is obvious that the different groups do not agree in value, which is shown better in the plot below.

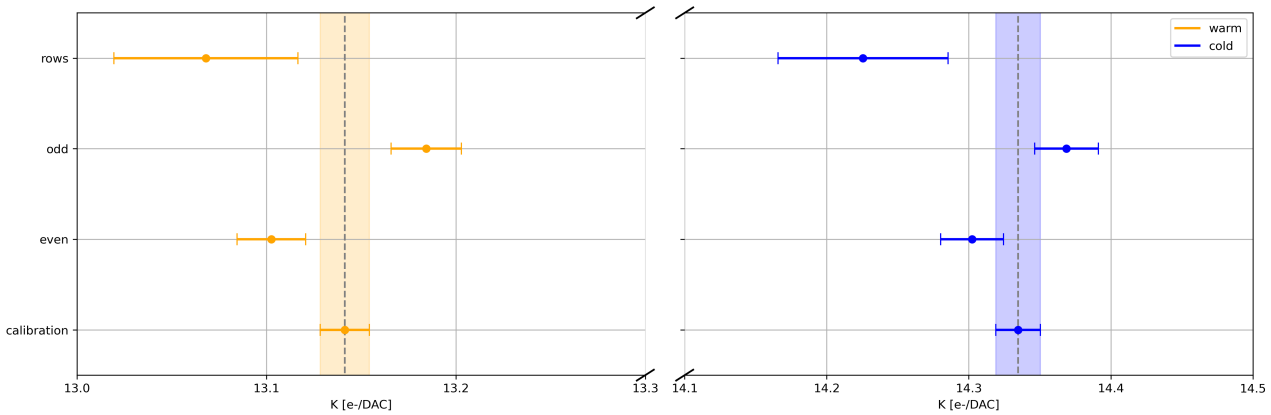

Figure 32: Summary of gain K[e-/DAC] values and uncertainties compared to the separated categories.

From Fig. 32, it is clear that the mean gain of the various groups considered differ from the mean of the main/calibration dataset when there is no separation in groups. This shows that there is a bias coming from the pixel position, shown with the various groups of pixels.

The equalisation process has been improved for the data acquisition system used by the full VELO detector(MiniDAQ3). This system runs on different firmware and software, fixing this apparent bias. Implementing all the improvements on the MiniDAQ2 system as well cannot be justified given the available person power, resources and limited used case. Therefore, it would be of interest to repeat this same separation in groups with new data taken using the MiniDAQ3 and the new equalisation process to ensure that this bias is not present.

6 Results

6.1 Measurements on the Gain K[e-/DAC] and Comparison to Estimate

This study has shown insights into the determination of the mean gain of the Velopix pixels when exposed to irradiation from a Fe55 source, analysed at two Module temperatures. The found values for the conversion factor or gain corresponding to each dataset are summarized in the table below.

Label	Module Temp.	ASIC	Total time(h)	Gain K_{mean} [e-/DAC]
Cold	-20°C	VP3-1	4.36	$14.33 \pm 0.02 \pm 0.16$
Warm	20°C	VP3-1	8.73	$13.14 \pm 0.01 \pm 0.44$

Table 3: Details concerning the datasets including the found results for the gain.

The higher gain found at lower Module temperatures can be understood as the pixels being more responsive at such conditions, which can be relevant information for the calibration and optimization of the Velopix for its correct operation.

From Figure 33, one can verify the compatibility of the mean gain measurements from the datasets considered to the paper estimate K_{est} [e-/DAC] $= 15.45 \pm 0.51$ [4]. The distance in number of standard deviations between them is calculated. The *warm* mean gain lies further than that of the *cold*, so the comparison is made to the latter value. The *cold* mean gain and the paper estimate are found to deviate from each other with 2.07 σ. This shows that the mean gain obtained from the *cold* measurements is somewhat compatible to the estimate given by the paper.

It is possible that with a further reduction of temperatures closer to those reached at LHCb when the detector is operational, the mean gain found would be closer to that given by the paper estimate. Nevertheless, this cannot be verified or extrapolated since only two temperatures were considered in this analysis.

6.2 Mean pixel vs ASIC Gain

The figure below shows the gain found by the calibration dataset, including the mean, ASIC and ASICgood values and associated uncertainties. The ASIC and ASICgood gains are plotted in red and purple respectively underneath the mean gain found by each dataset, such that the comparison of these values becomes more readily apparent. The gain estimate predicted by the VeloPix ASIC design paper [4] is included in green.

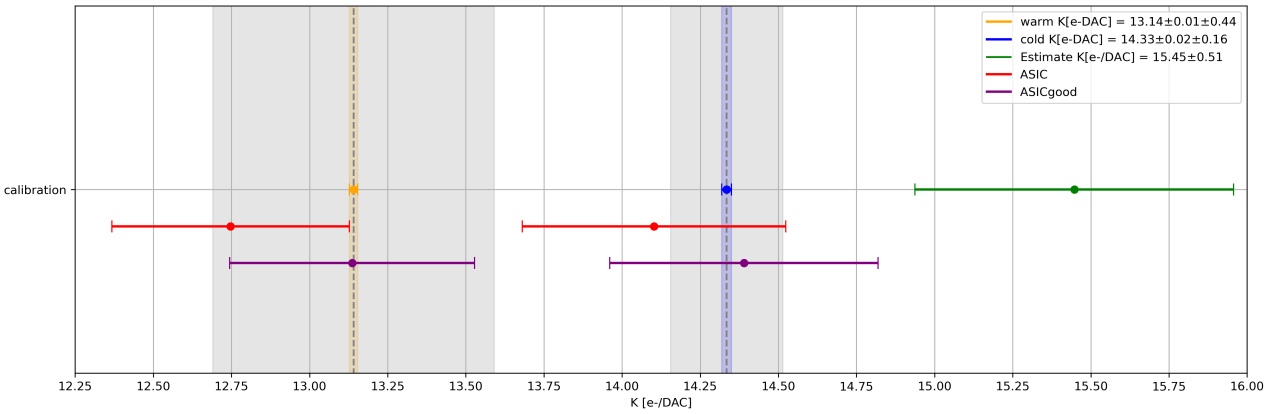

Figure 33: Mean, ASIC and ASICgood gain values for the *cold* and *warm* dataset. The mean gain and its statistical uncertainty are plotted in yellow for *warm* and in blue *cold* dataset. The systematic uncertainty shown as a grey band for each gain measurement. Values obtained from Table 6.1. Estimated gain from paper in green.

The *warm* ASIC gain is slightly separated from the mean gain found by the dataset. Even including its error bar does not exactly allow these two results to be compatible with each other, which is only the case in the *cold*

dataset. It is the systematic uncertainty associated to the means that allow the ASIC gain to be in agreement with the mean gain for both datasets, although this was already the case in *cold* measurements. The bias from *bad* pixels is still embedded within the found ASIC gain, yet still making a good prediction of the mean gain for a given dataset.

The ASICgood gain found by each dataset is obviously lying really close to that of the mean. The gain is computed as the inverse of the target E_t up to some proportionality constant. From this, it is obvious that the mean of the targets found by the various pixels and the ASICgood target, which comes from the fit to the average flux curve, will find values close to each other since they should be equivalent approaches. The disagreement among the mean and ASICgood might come from issues in the inclusion of the noise baseline position during the data analysis, or from the clear fitting issues shown in Fig. 4.1.1.

From this, it is possible to confirm that the ASIC gain does make a decently good prediction for the mean gain of the dataset, since there is agreement within the uncertainties explored. This becomes of importance if further studies on irradiation to the ASICs are performed, from which the ASIC gain can be used to have a fast prediction of the mean gain rather than performing the analysis over all the pixels, which can become time-consuming depending on the quantity of data and specifics of the analysis applied.

7 Conclusions

7.1 Summary of Findings

The analysis has shown a distinct variation in the mean gain of the Velopix pixels when using different Module temperatures when irradiated by X-rays from a Fe55 source. The mean gain for the VP3-1 ASIC was found to be higher for the *cold* dataset, with a value of 14.33 ± 0.02 (stat) ± 0.16 (syst) [e-/DAC] at -20°C, compared to the gain of the *warm* dataset, which found 13.14 ± 0.01 (stat) ± 0.44 (syst) [e-/DAC] at a Module temperature of 20°C. The systematic uncertainty was determined from investigation of the exposure time influence of the ASIC to the radiation source.

Various flux models were considered to fit the data. It is concluded, based on the residuals and pulls, that the best flux model is that of Eq. 4, and that the model fits decently well to the individual pixels but does not describe accurately the average flux curve of the ASIC in specific threshold regions.

Another measure of the average behaviour has been explored using the ASIC value, introduced in Sec. 3.4. From the results shown in Sec. 6.2, comparing the mean and ASIC gain within uncertainties, it is established that the ASIC average flux can indeed provide reliable information on the gain of the pixels. This can be of use for reasons explained in Sec. 4.7

Furthermore, it has been established that Module temperature is a major influence regarding the categorisation of pixels in the data processing, and that exposure time does have an impact on the data, from which a systematic uncertainty has been assigned to the mean gain measurements. Positional bias between pixels in even and odd columns has been investigated, and its presence is confirmed when looking at the mean gain of the pixels.

Last but not least, this study required the analysis of datasets, from which all the presented results and plots were obtained. This was made possible by development of a Python framework for analysing datasets from irradiation tests on ASICs from the Velopix, which can be modified and extended further for future radiation studies on the detector.

7.2 Outlook

This study has provided insights into the determination of the mean gain of a Velopix ASIC pixels under irradiation. However, there are several areas which remain open for further investigation.

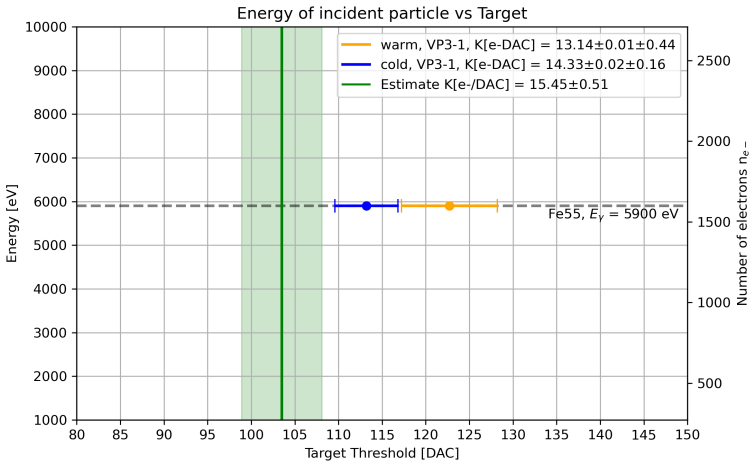

Figure 34: Energy of incident radiated particle vs target E_t in DAC units. The mean gains found by the *cold* and *warm* dataset are shown. The error bars represent the combined uncertainties by quadrature. The green vertical line represents the Estimate from paper while the horizontal dashed line shows the energy of the source used for this analysis as well as the energy of its X-rays. The y-axis represent energy deposited in eV and in number of electrons n_{e^-} for better comprehension.

Since a code framework for this analysis has been developed, it can now be used to conduct comparative studies. Using various radiation sources and other ASICs, these becoming extra measures for Figure 34, providing insights on the dissimilarities and performance of the different ASICs considered.

The flux model used throughout this analysis can be improved, specially if one wants to model the average flux on the ASIC accurately. Exploring other models to fit the measurements of the overall ASIC flux could provide a better understanding of physical processes or influences that might have not been taken into account for this analysis.

The positional bias between pixels in even and odd columns has been observed in Sec. 5.2, and it is likely due to not utilizing the latest developments in the equalisation process. Therefore, it would be suitable for future irradiation studies if the data taking is done with the MiniDAQ3 and using the new equalisation process, with hopes of improved data acquisition measurements and a fix for the positional bias.

While the systematic uncertainty was obtained from the exposure time variation, a more detailed investigation into the relation between exposure time and data quality or gain measurements will be valuable. Measurements with greater exposure times and variability in the number of acquisitions or shutter time used might provide useful information for a more precise assessment of the systematic uncertainty.

It would also be interesting to investigate a wider range of temperatures, specially closer to the operational conditions at LHCb (at <-30°C), since the lowest Module temperature used in one of the datasets is -20°C. This could help to verify if the mean pixel gain of the ASIC does converge to that of the estimated gain from [4].

8 Acknowledgments

I would like to thank my supervisor Kristof De Bruyn for the opportunity to work in this project, and for the great guidance that he has provided.

MD for the data taking at Nikhef and for the support provided during this project.

Andrej and Daniel for the laughs and helpful advice.

The LHCb Groningen and VSI members for the chance to work among good colleagues and for the coffee breaks.

And thank you to my family and close friends for believing in me during my studies and time in Groningen.

Bibliography

[1] R. Aaij *et al.* [LHCb], "The LHCb Upgrade I," JINST **19** (2024) no.05, P05065 doi:10.1088/1748-0221/19/05/P05065 [arXiv:2305.10515 [hep-ex]].

[2] M. van Beuzekom, J. Buytaert, M. Campbell, P. Collins, V. Gromov, R. Kluit, X. Llopart, T. Poikela, K. Wyllie and V. Zivkovic, "VeloPix ASIC development for LHCb VELO upgrade," Nucl. Instrum. Meth. A **731** (2013), 92-96 doi:10.1016/j.nima.2013.04.016

[3] J. Visser, M. v. Beuzekom, H. Boterenbrood, B. v. d. Heijden, J. I. Muñoz, S. Kulis, B. Munneke and F. Schreuder, "SPIDR: a read-out system for Medipix3 & Timepix3," JINST **10** (2015) no.12, C12028 doi:10.1088/1748-0221/10/12/C12028

[4] T. Poikela, R. Ballabriga, J. Buytaert, X. Llopart, W. Wong, M. Campbell, K. Wyllie, M. van Beuzekom, J. Schipper and S. Miryala, *et al.* "The VeloPix ASIC," JINST **12** (2017) no.01, C01070 doi:10.1088/1748-0221/12/01/C01070

[5] M. Urban *et al.* "Timepix3: Temperature influence on radiation energy measurement with Si Sensor." Sensors, 23(4), p. 2201. (2023) doi:10.3390/s23042201.

[6] International Atomic Energy Agency (IAEA). (n.d.). *LiveChart of Nuclides*. Retrieved July 7, 2024, from `https://www-nds.iaea.org/relnsd/vcharthtml/VChartHTML.html`

[7] H. Kolanoski and N. Wermes, "Particle Detectors," Oxford University Press, 2020, ISBN 978-0-19-885836-2

[8] E. A. Papadelis, "Characterisation and Commissioning of the LHCb VELO Detector," CERN-THESIS-2009-044.

[9] J. Fang et al., "Understanding the Average Electron–Hole Pair-Creation Energy in Silicon and Germanium Based on Full-Band Monte Carlo Simulations," in IEEE Transactions on Nuclear Science, vol. 66, no. 1, pp. 444-451, Jan. 2019, doi: 10.1109/TNS.2018.2879593.

[10] M. N. Mazziotta., "Electron–hole pair creation energy and Fano factor temperature dependence in silicon." in Nuclear Instruments and Methods in Physics Research Section A: Accelerators, Spectrometers, Detectors and Associated Equipment, 584(2-3), 436–439. (2008) doi:10.1016/j.nima.2007.10.043

[11] A. Biolchini and P. Kopciewicz, "Equalisation Backend Notes" `https://codimd.web.cern.ch/s/mIhC4Lvj5`

[12] M.D. Galati, 'VeloPix Fe55 threshold scan (presentation Nikhef Velo meeting)'. `https://indico.nikhef.nl/event/3984/contributions/15020/attachments/6403/8302/2022-11-01%20VeloPix%20Fe55%20threshold%20scan.pdf`

[13] M.D. Galati, 'Threshold scans (presentation Nikhef Velo meeting)'. `https://indico.nikhef.nl/event/4645/contributions/17856/attachments/7301/9858/2023-08-23%20Threshold%20scans.pdf`

Appendix

A Error propagation

The uncertainty on the average number of ehp created n_{ehp} is derived from Eq.14 to be,

$$\Delta n_{ehp} = n_{ehp}\sqrt{\left(\frac{\Delta E_\gamma}{E_\gamma}\right)^2 + \left(\frac{\Delta E_{ehp}}{E_{ehp}}\right)^2} = n_{ehp}\left(\frac{\Delta E_{ehp}}{E_{ehp}}\right) \tag{19}$$

The uncertainty related to the average ehp creation energy E_{ehp} has to be taken into account, however, since ΔE_γ is much smaller than ΔE_{ehp}, it is neglected. This can then be used to find the uncertainty related to the conversion factor K from Eq. 15,

$$\Delta K = K\sqrt{\left(\frac{\Delta n_{ehp}}{n_{ehp}}\right)^2 + \left(\frac{\Delta E_t}{E_t}\right)^2} \tag{20}$$

Some extra error propagation was needed to combine the statistical and systematic uncertainties found by the mean gain, shown in 34.

$$\Delta K_{total} = \sqrt{(\Delta K_{stat})^2 + (\Delta K_{sys})^2} \tag{21}$$

and then converted to a target value using,

$$\Delta E_t = E_t\sqrt{\left(\frac{\Delta n_{ehp}}{n_{ehp}}\right)^2 + \left(\frac{\Delta K_{total}}{K_{total}}\right)^2} \tag{22}$$

B Parameter Heatmaps

Note: the average of the corresponding parameter is shown on the title of the graph, this being calculated taking into account a weight for each individual value found to be $w_i = 1/(\sigma_i)^2$, with σ_i being the uncertainty related to the parameter at said pixel. This choice for the weight of each individual value is not arbitrary, but rather the value such that the mean maximizes the Maximum Likelihood estimator.

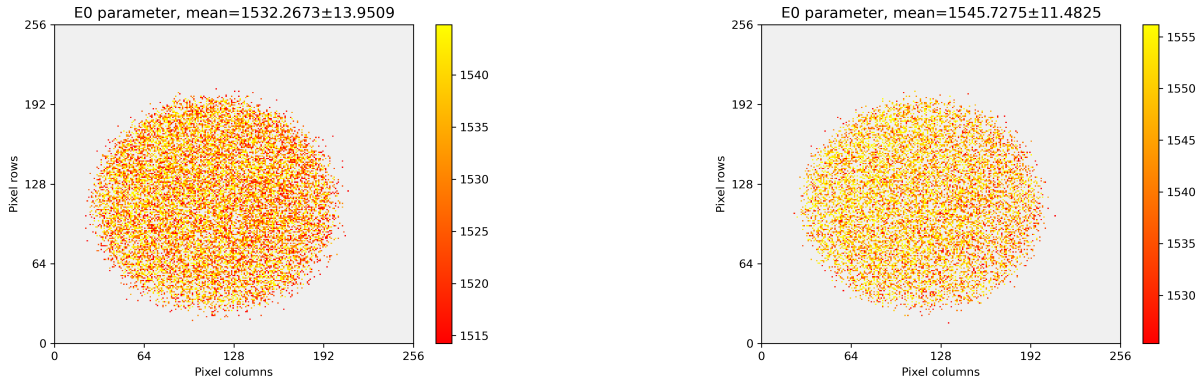

(a) Cold dataset.

(b) Warm dataset.

Figure 35: Heatmaps of E_0.

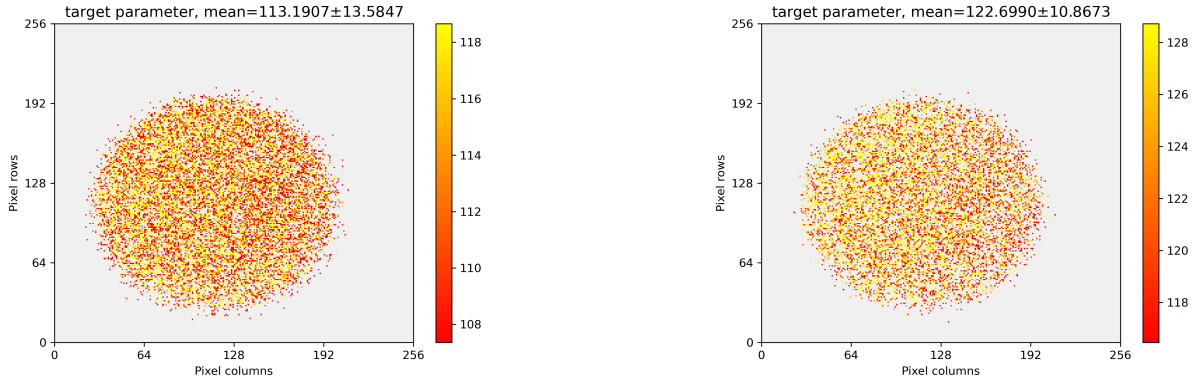

(a) Cold dataset.

(b) Warm dataset.

Figure 36: Heatmaps of target.

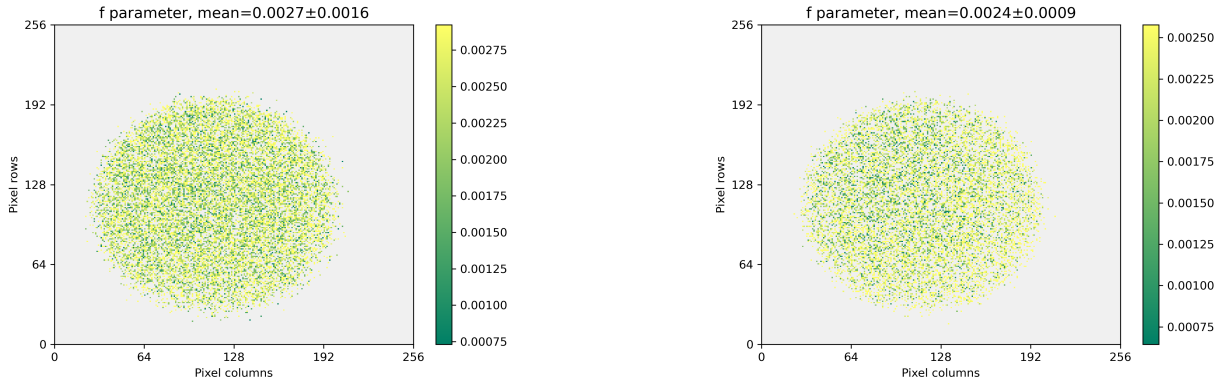

(a) Cold dataset. (b) Warm dataset.

Figure 37: Heatmaps of f.

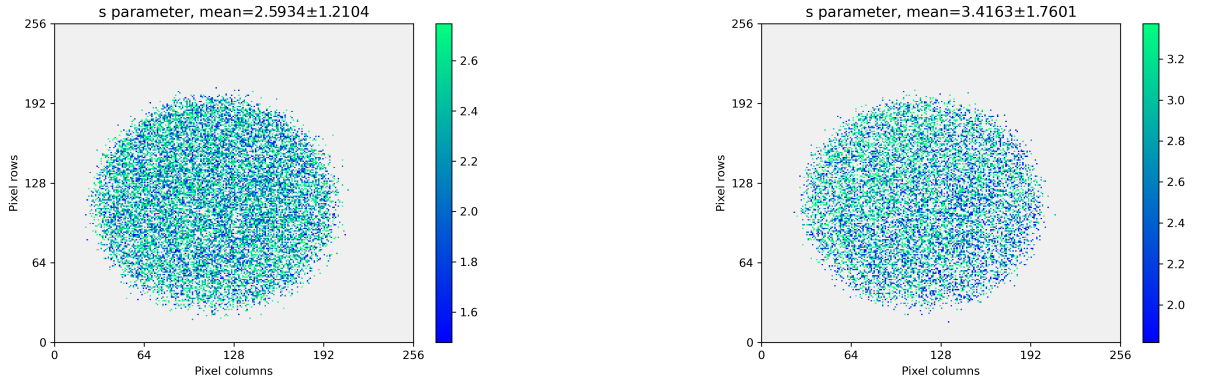

(a) Cold dataset. (b) Warm dataset.

Figure 38: Heatmaps of s.

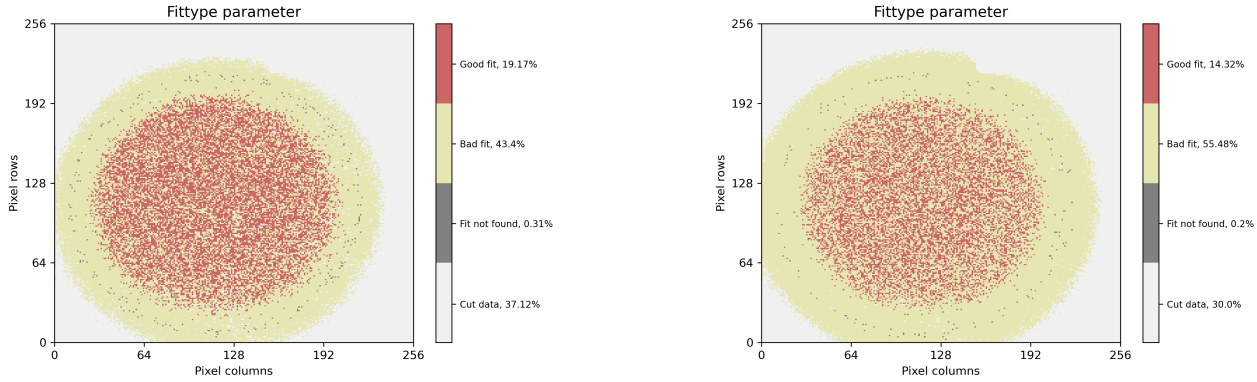

(a) Cold dataset. (b) Warm dataset.

Figure 39: Heatmaps of Fit type.

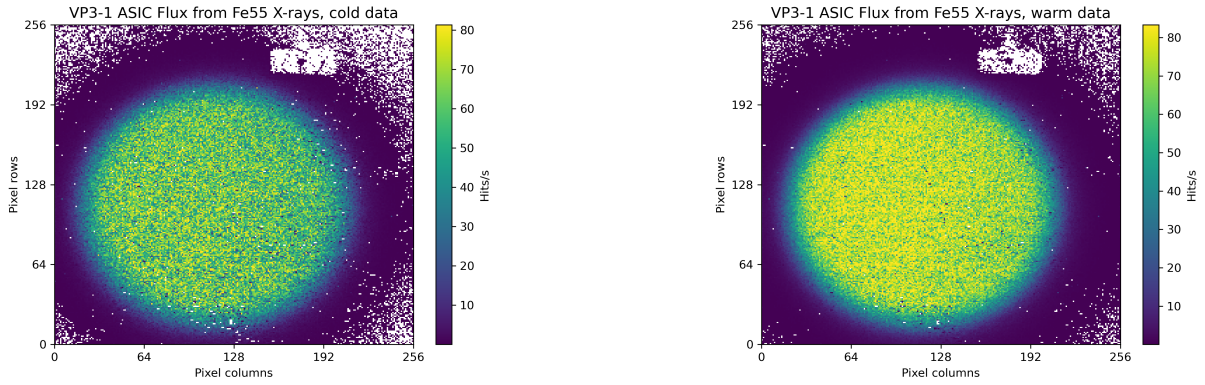

(a) Cold dataset.

(b) Warm dataset.

Figure 40: Heatmaps of Flux summed over all thresholds. Includes mask of pixels which flux <= 0.

An important note to be made is the fact that there is a small dent observable in the fit type heat map Fig. 18 in the upper right perimeter of the *bad fit* pixel circle. This can be explained by a lack of flux coming from this very same area within the ASIC, as it can be seen from the flux heatmaps shown in Fig. 39, where the flux was masked if it was less or equal than 0. It is possible that there was an object covering that specific area during irradiation and therefore did not receive any hits.

C On the Fit Not Found Ring

As previously mentioned in Sec. 4.2, there is a certain structure which can be observed in the heatmap representation of the ASIC, more explicitly regarding the category assigned to each of the individual pixel during the data analysis. A circular pattern for the various categories considered can be seen, as well as the appearance of a ring, lying at some distance from the centre of the ASIC, which exclusively corresponds to those pixels that were assigned the *fit not found* category.

Since various flux equations have been introduced in Sec. 2.1.2 and used to run the data analysis, it might be possible to obtain insights regarding the appearance of this *fit not found* ring. The flux equations $F_{3,0}$ and F_3, given by Eqs. 8 and 9 respectively, provide similar results while still having minor differences on their structure compared to that of the original flux equation $F_{1,0}$ and F_1. This can be exploited to try to obtain insights on the appearance of said ring, if it is closely associated to some factor involved in the equation which makes the fit diverge more easily. The fit type heatmaps for the various flux equations are shown below, with the percentage of pixels in each category displayed next to the colour bar.

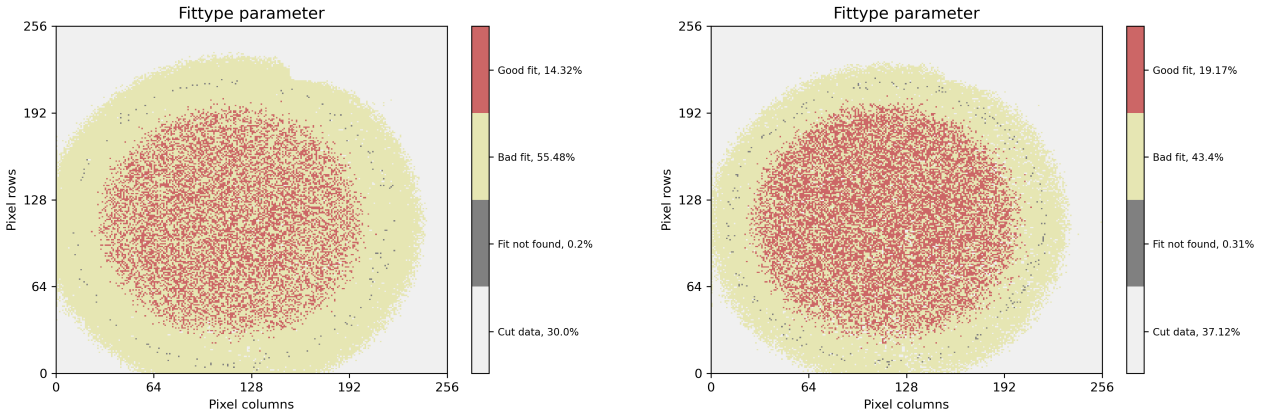

(a) Warm (b) Cold

Figure 41: Comparison of fittype for calibration $F_{1,0}$

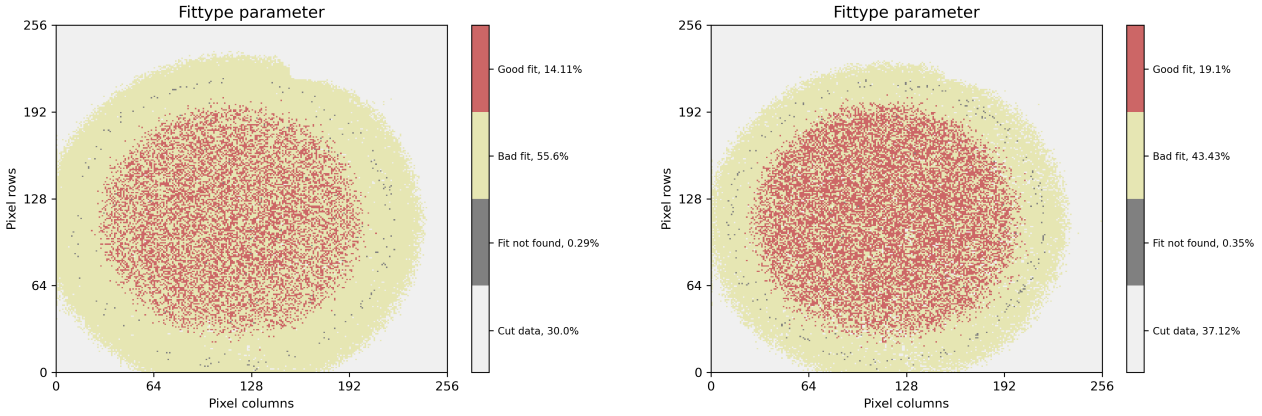

(a) Warm (b) Cold

Figure 42: Comparison of fittype for calibration no term0 F_1

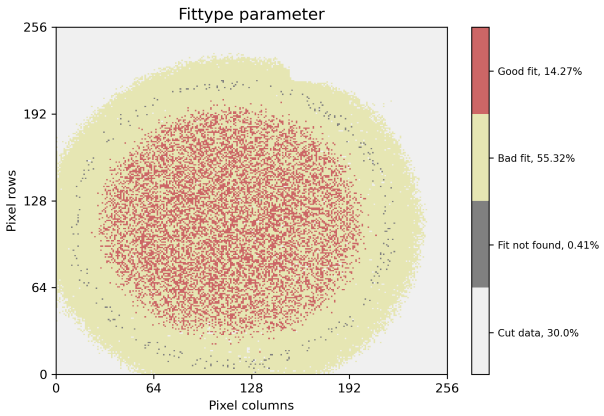

(a) Warm

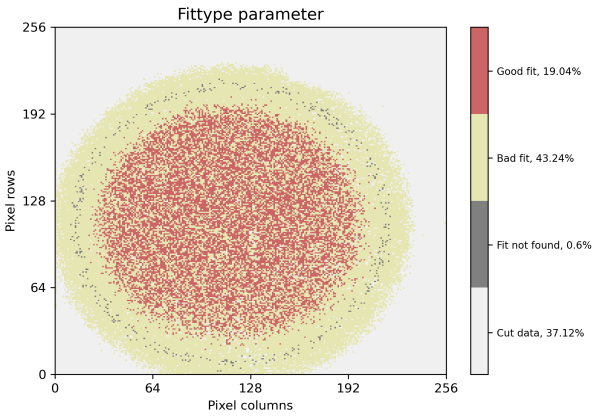

(b) Cold

Figure 43: Comparison of fittype for $F_{AB,0}$

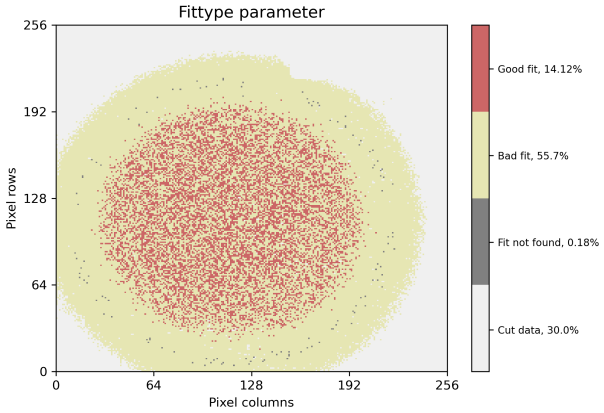

(a) Warm

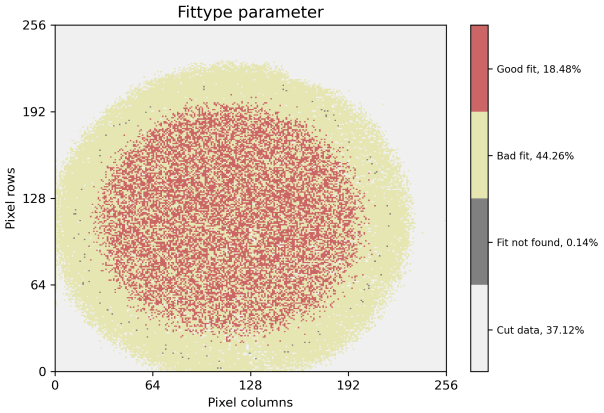

(b) Cold

Figure 44: Comparison of fittype for F_{AB}

It is very difficult to obtain any insights from direct observation and comparison of these plots. For an easier comparison, an overlay of these heat maps could be performed such that the differences in the pixel categorisation become more prominent. Overlaying the various fit functions used on the flux data points of the individual pixels could also provide insights in this topic. It is possible that this is an accidental result coming from the fitter section of the code, due to how your fitter decides when the fit converged or not.

This was not explored further in the analysis shown and left as remark for possible future irradiation studies performed.

D Approaches on baseline inclusion

Since the analysis relies on the calculation of the target, the inclusion of the baseline is certainly important for the calculations. The two approaches taken throughout the above analysis as well as an extra are described below:

- calibration/main: Approach explored so far. Get E_0, $\rightarrow$ target $= E_0 - E_b$, error propagation needed for uncertainty. Uses ASICbaseline $= \overline{baseline_{i,j}}$ for target$_{ASIC}$

- baseline_while_fit: Get target directly from fit, the shift is performed on the Threshold range. No need for error propagation, uncertainty comes from fit.

- newbaseline: baseline shift included in generation of Flux files.

The second approach, baseline_while_fit, uses the information of the baseline for each individual pixel to shift the original threshold range in which the data is taken to a new threshold range, *thrshift*. This is done for all of the pixels and their target as well as uncertainty is obtained from here. The ASIC value is still considered in the same way as in calibration/main approach, the hits from all the pixels are summed over the original threshold range, but then it is shifted by baseline$_{ASIC}$ before performing the fit from which the target is obtained. This is the approach from which the final results described in Sec. 2.5 are calculated.

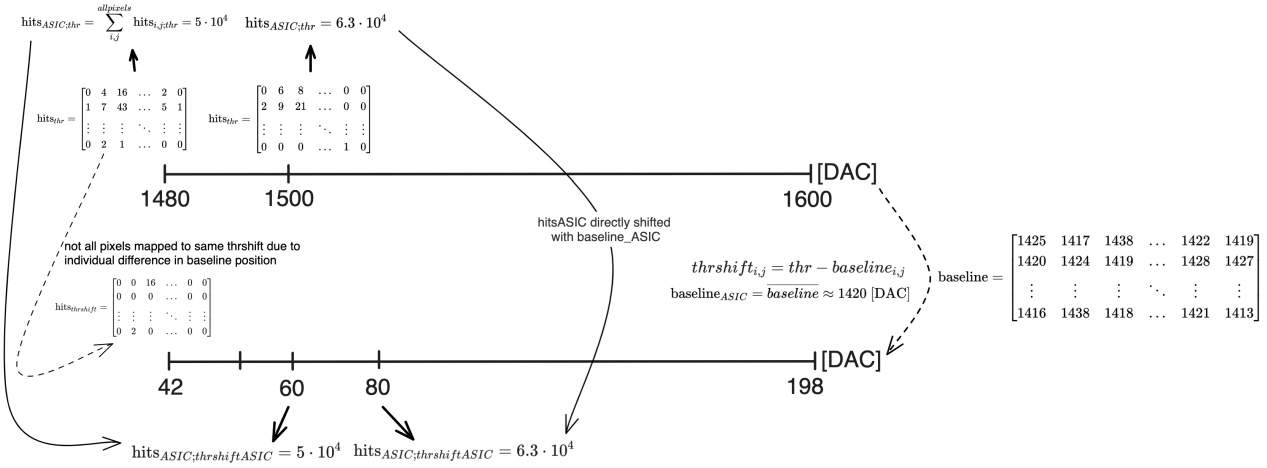

Figure 45: Calibration baseline while fit approach schematic. Each individual pixel is mapped to the new thrshift line by their corresponding baseline position. The ASIC hits are calculated on the original threshold range, and then the ASIC flux is mapped with the average of all the pixel baselines.

The third approach, named *newbaseline*, introduces a new way of finding the ASIC value. This value is calculated by summing over the hits from all pixels at a certain threshold in the *thrshift* range, after all the pixels have been remapped. This leads to a possibly more accurate measure of the ASIC/average value.

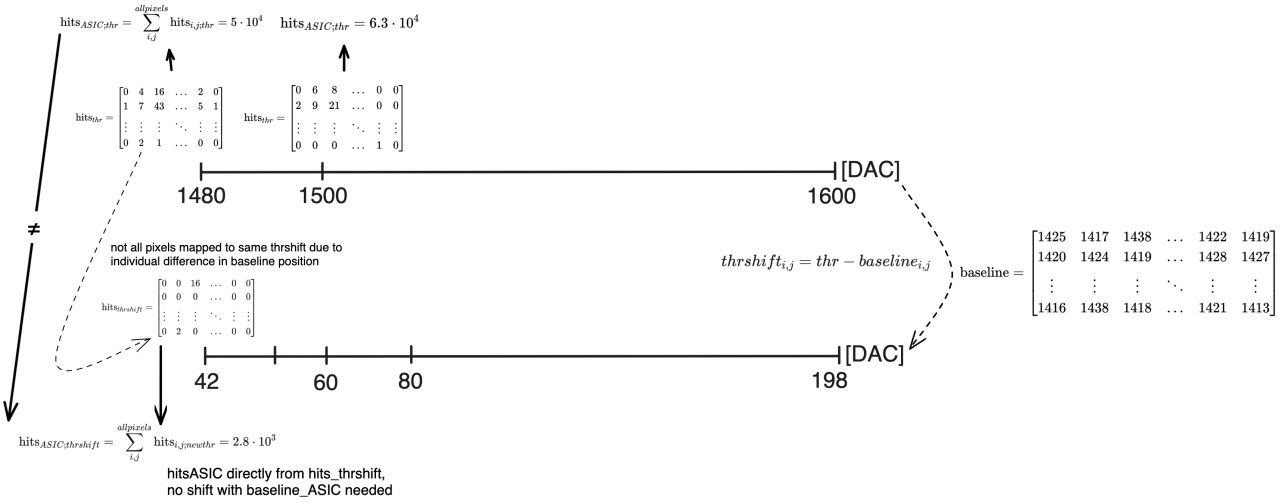

Figure 46: Newbaseline approach schematic. Same a the previous approach shown, expect in this one, the ASIC flux is calculated after the pixels have been mapped to the thrshift line, leading to difference ASIC fluxes.

Nevertheless, the *newbaseline* approach also has its imperfections. Since not all the pixels agree on where their corresponding noise baseline position lies, there will be very few pixels being mapped to the extremes of *thrshift*, leading to less pixels to sum their hits over and thus, the ASIC flux curve does not look the same in the low threshold range to that of the flux curve in the two other approaches. This can be fixed in a 'manual' way by including a cutoff in the code such that the fit over this ASIC flux curve is performed from the *thrshift* value at which the ASIC flux peaks and starts to decrease. The objective of this newbaseline approach is to also correct for the pixel to pixel variations, with the introduction of the individual baselines as aforementioned, which can be observed by comparing the ASIC flux curve from the other two approaches to that found in this one, as shown in the figure below.

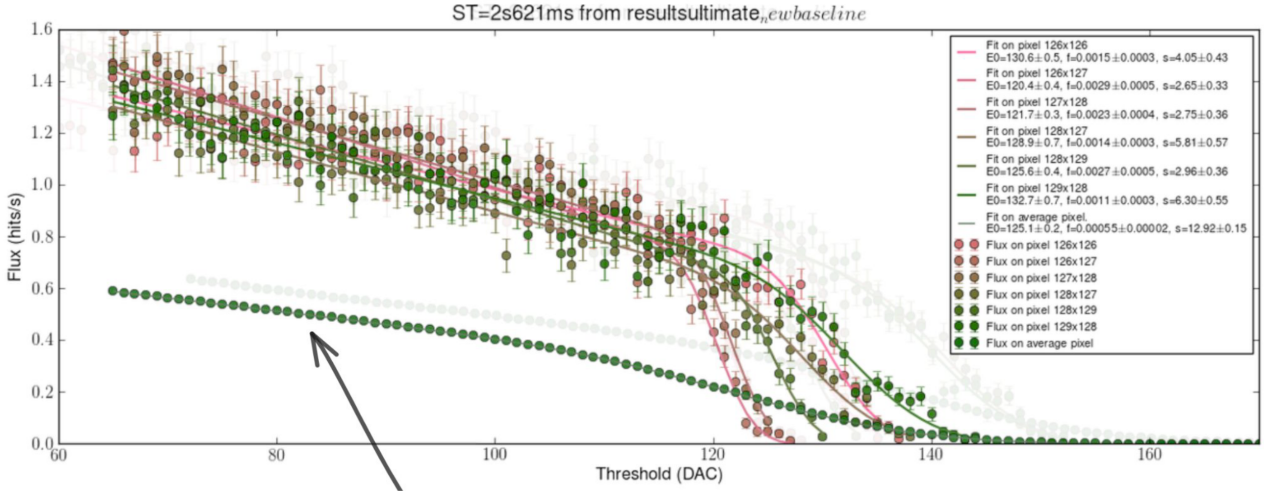

Figure 47: Comparison of ASIC flux curve from calibration/main vs newbaseline. The dim curves and datapoints in the background are that of the calibration approach, while the more prominent are from newbaseline. CHANGE GRAPH AND MAKE IT MORE NEATLY.

As it can be observed, the ASIC curve presents a slightly sharper drop in flux, this coming from the baseline corrections, since the disagreement of pixels on the value of E_0 made the curve smoother than it should. The pixels still exhibit differences regarding the value of the target, as it can be seen from the individual pixels plotted, this being due to the statistical nature of the X-ray detection by the ASIC/pixel's energy resolution, related to the s parameter in the flux equation Eq. 4.

Regarding these two first approaches, subtracting the baseline value from the E_0 value after the fit should lead to exactly the same results as if the baseline is subtracted right before performing the fit on the flux for the pixels, since both are mathematically equivalent. Therefore, the results coming out from these two approaches should not be different, which is observed in the values from Fig. 48. The mean and ASIC for both approaches are the same, only differing in the uncertainty of the ASIC values considered, since it comes directly from the fit to the flux curve.

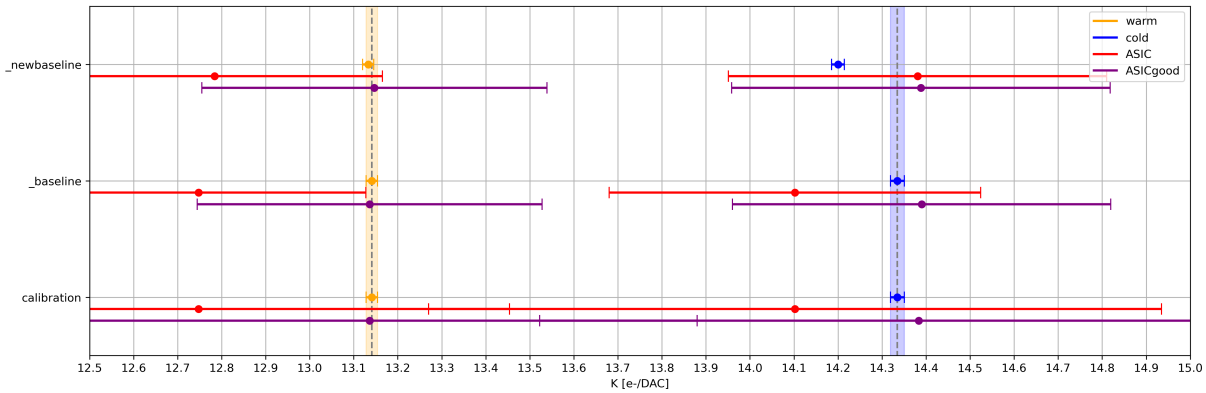

Figure 48: Summary of K[e-/DAC] results from the various approaches considered. The mean and its associated error is shown together with the ASIC and ASICgood values. Both the *warm* and *cold* datasets are represented.

When looking at the results coming from the newbaseline approach, it is easy to see from Fig. 48, that its K[e-/DAC] ASIC value now seems to be making a closer prediction to the mean of the calibration/main approach, which is assumed to be the most accurate representation of the data. This is true for the cold dataset, since the warm data seems to still be lying off from the mean of calibration/main approach, but with its uncertainty being within the mean value. The mean of this newbaseline approach seems to be finding a slightly lower value for the *cold* dataset compared to the calibration/main approach, even thought both should have found the same value. This thought to come from a possible error on the analysis code.

Since not too many insights were obtained from exploring the introduction of the baseline shift with another approach, this is left as a remark for future studies. The results here presented are not shown throughout the rest of the study.